Pathological mutations reveal the key role of the cytosolic iRhom2 N-terminus for phosphorylation-independent 14-3-3 interaction and ADAM17 binding, stability, and activity.

Katharina Bläsius[1*], Lena Ludwig[1*], Sarah Knapp[2], Charlotte Flaßhove[1], Friederike Sonnabend[1], Diandra Keller[1], Nikola Tacken[1], Xintong Gao[1], Selcan Kahveci-Türköz[1], Caroline Grannemann[1], Aaron Babendreyer[1], Colin Adrain[3], Sebastian Huth[4], Jens Malte Baron[4], Andreas Ludwig[1], Stefan Düsterhöft[1#]

[1] Institute of Molecular Pharmacology, Medical Faculty, RWTH Aachen University, Aachen, Germany

[2] Institute of Biochemistry and Molecular Biology, Medical Faculty, RWTH Aachen University, Aachen, Germany

[3] Patrick G Johnston Centre for Cancer Research, Queen's University, Belfast, N. Ireland

[4] Department of Dermatology and Allergology, Medical Faculty, RWTH Aachen University, Aachen, Germany

corresponding author

* authors contributed equally

Abstract

The protease ADAM17 plays an important role in inflammation and cancer and is regulated by iRhom2. Mutations in the cytosolic N-terminus of human iRhom2 cause tylosis with oesophageal cancer (TOC). In mice, partial deletion of the N-terminus results in a curly hair phenotype (cub). These pathological consequences are consistent with our findings that iRhom2 is highly expressed in keratinocytes and in oesophageal cancer. Cub and TOC are associated with hyperactivation of ADAM17-dependent EGFR signalling. However, the underlying molecular mechanisms are not understood. We have identified a non-canonical, phosphorylation-independent 14-3-3 interaction site that encompasses all known TOC mutations. Disruption of this site dysregulates ADAM17 activity. The larger cub deletion also includes the TOC site and thus also dysregulated ADAM17 activity. The cub deletion, but not the TOC mutation, also causes severe reductions in stimulated shedding, binding, and stability of ADAM17, demonstrating the presence of additional regulatory sites in the N-terminus of iRhom2. Overall, this study contrasts the TOC and cub mutations, illustrates their different molecular consequences, and reveals important key functions of the iRhom2 N-terminus in regulating ADAM17.

Key words: esophageal squamous cancer, ectodomain shedding, EGFR ligand release, curly-bare (cub) mouse, iRhom2, ADAM17, Howel–Evans syndrome, tylosis with oesophageal cancer (TOC), 14-3-3 proteins, stratifin

Introduction

Oesophageal cancer (OC) is a critical global health concern, given its alarming prognosis and high mortality rate, ranking as the sixth leading cause of cancer-related death worldwide. Oesophageal squamous cell carcinoma (OSCC) and oesophageal adenocarcinoma (OAC) are the primary histological subtypes of OC. Despite their similarities, OSCC and OAC differ both epidemiologically and biologically (Rizza et al., 2015, Smyth et al., 2017, Uhlenhopp et al., 2020). The prognosis for OSCC, which comprises most OC cases, is exceptionally poor (Uhlenhopp et al., 2020, Yang et al., 2022). Notably, smoking and alcohol consumption serve as significant risk factors for OSCC development. However, the underlying molecular and genetic mechanisms driving OC remain poorly understood.

Howel-Evans syndrome, also called tylosis with oesophageal carcinoma (TOC), directly correlates with an increased risk to develop OSCC (Howel-Evans et al., 1958, Blaydon et al., 2012). This rare genetic disorder affects the seven-transmembrane spanning pseudoprotease iRhom2 (Fig. 1A) and its functions, altering EGF receptor (EGFR) signalling pathways by aggravating iRhom2-dependent ectodomain shedding (Blaydon et al., 2012).

Shedding, the proteolytic release of ectodomains from membrane proteins, is a crucial mechanism in many physiological and pathological processes. The released soluble ectodomains, which are often receptors or receptor ligands, exhibit potent biological activity. iRhoms, pseudoproteases of the rhomboid family, play a crucial role in the shedding process by forming a complex with the transmembrane sheddase ADAM17 (A-disintegrin and metalloproteinase 17)(Siggs et al., 2012, Christova et al., 2013, Siggs et al., 2014, Li et al., 2015).

ADAM17 has a broad spectrum of substrates, including cytokines, growth factors and cytokine receptors such as tumour necrosis factor (TNF)(Black et al., 1997), transforming growth factor α (TGFα) and amphiregulin (AREG)(Peschon et al., 1998, Sahin et al., 2004). Release of these substrates is crucially involved in various (patho-)physiological processes (Peschon et al., 1998, Blaydon et al., 2011) highlighting the central role of ADAM17 in development and in the immune response but also in chronic inflammation and cancer. Additionally, the multi-faceted role of ADAM17 in virus entry has been recently demonstrated (Lambert et al., 2005, Palau et al., 2020, Yuan et al., 2021, Jocher et al., 2022, Niehues et al., 2022, Zaruba et al., 2022).

The formation of the iRhom-ADAM17 complex is a necessary step for ADAM17 maturation (Fig. 1A,B)(Christova et al., 2013, Maretzky et al., 2013, Grieve et al., 2017, Düsterhöft et al., 2021, Kahveci-Türköz et al., 2023). On the cell surface the shedding activity of mature ADAM17 is further regulated by iRhoms (Cavadas et al., 2017, Grieve et al., 2017). In mammals, two genes for iRhoms exist: RHBDF1 (iRhom1) and RHBDF2 (iRhom2). While iRhom1 is present in most cell types, iRhom2 initially appeared to be immune cell specific, but is also upregulated during inflammatory episodes in

71 other cell lineages such as endothelial and epithelial cells (Lu et al., 2017, Babendreyer et al., 2020,
72 Giese et al., 2021). Consistent with this, iRhom2 deficiency in mice and humans does not cause obvious
73 developmental defects, but impairs the immune response (Adrain et al., 2012, McIlwain et al., 2012,
74 Kubo et al., 2022).

75 iRhoms contain a large N-terminal cytosolic tail that has not yet been fully characterised (Fig. 1A). The
76 genetic disorder causing TOC is caused by single point mutations in the N-terminus (Howel-Evans et
77 al., 1958, Ellis et al., 1994, Blaydon et al., 2012, Saarinen et al., 2012, Ellis et al., 2015, Mokoena et al.,
78 2018). This disorder is characterised by symptoms such as leukoplakia and hyperkeratosis and
79 increases the risk of OSCC (Chao-Chu et al., 2021). The mutations are classified as "gain of function"
80 because they apparently upregulate ADAM17 activity, resulting in higher levels of EGFR ligands, EGFR
81 hyperactivation in keratinocytes and increased release of TNF receptor 1, leading to reduced apoptosis
82 (Blaydon et al., 2012, Maney et al., 2015, Hosur et al., 2018b).

83 In mice, a spontaneous mutation called cub (curly-bare) results in a deletion of 268 amino acid residues
84 of the N-terminus including the TOC mutation positions, causing aberrant hair growth, hyperkeratosis
85 and hyperproliferative wound healing (Johnson et al., 2003, Siggs et al., 2014, Hosur et al., 2018a). This
86 cub deletion was linked to higher ADAM17-mediated shedding of AREG. However, different studies
87 contested the notion that the cub mutation results in higher ADAM17 activity at least in *in vitro* settings
88 (Siggs et al., 2014, Hosur et al., 2018a). Interestingly, mice carrying TOC mutations exhibit the same
89 skin-related phenotype as cub mice (Hosur et al., 2017, Hosur et al., 2018a, Hosur et al., 2018b).
90 Noteworthy, the deficiency in iRhom2 in mice seems to cause a thinning of epidermis in the footpad
91 (Maruthappu et al., 2017). The phenotype of both, cub and TOC mice, can be rescued by AREG
92 deficiency, suggesting a similar underlying process with increased AREG-dependent signalling (Hosur
93 et al., 2018b). However, the molecular mechanism for these mutations remains unknown.

94 Only a few regulatory regions have been identified within the N-terminus of iRhom2, including
95 phosphorylation sites that facilitate phosphorylation-dependent binding of members of the 14-3-3
96 protein family (Cavadas et al., 2017, Grieve et al., 2017). Deletion of the entire N-terminus appears to
97 destabilise the iRhom-ADAM17 complex, resulting in loss of mature ADAM17. The adapter protein
98 FRMD8, also known as iTAP (iRhom tail-associated protein) has been identified as an essential binding
99 partner of the N-terminus of iRhom, which has a stabilising function for iRhom and thus for the iRhom-
100 ADAM17 complex (Künzel et al., 2018, Oikonomidi et al., 2018). This seems to explain the loss of
101 mature ADAM17 when the N-terminus is missing. Notably, part of this FRMD8-binding region is lost in
102 the cub deletion, while the TOC mutations lie outside this region. Recently, it was shown that the N-
103 terminus is cleaved off by a signal peptidase complex and migrates to the nucleus, where it influences
104 gene expression (Dulloo et al., 2022, Zanotti et al., 2022).

105 In this study, we observed high expression levels of iRhom2 in skin tissue samples and primary
106 keratinocytes under physiological conditions, providing an explanation for the distinct skin-related
107 phenotype in humans and mice with TOC or cub, respectively. Notably, iRhom2 and ADAM17
108 expression levels were significantly upregulated in OSCC patient samples, which is consistent with the
109 higher risk for OSCC in TOC patients.

110 It is important to separate the direct molecular effects of both mutation types (single point mutation
111 vs large deletion) on the functions of the iRhom2-ADAM17 complex from downstream effects: *In vivo*,
112 altered ADAM17 activity and the mutated soluble iRhom2 N-terminus in the nucleus will have long-
113 term effects on gene expression as well as ADAM17-dependent signalling pathways. Here, we focused
114 on the direct molecular consequences of the TOC single point mutations and the large cub deletion.
115 We identified a highly conserved motif that contains all known TOC sites and represents a
116 phosphorylation-independent 14-3-3 protein interaction site. Disruption of this site results in loss of
117 regulation of ADAM17 activity, leading to increased constitutive shedding. In contrast, the pathological
118 murine cub deletion covers a larger part of the N-terminus, including the TOC site. Therefore, the cub
119 deletion also causes higher constitutive shedding activity of ADAM17. However, the cub deletion loses
120 the ability to promote stimulated/activatable ADAM17 activity. In addition, we found that this deletion
121 decreases binding to ADAM17 and causes accelerated degradation of ADAM17.

122 Overall, our results provide deeper insights into the molecular mechanisms controlling the iRhom2-
123 ADAM17 complex through the N-terminus of iRhom2 by demonstrating a distinct effect of TOC site
124 disruption, in contrast to the multiple overlapping and therefore more severe effects of the cub
125 deletion.

126

127

128 ## Results

129

130 ### iRhom2 expression levels are high in skin and OSCC

131 The observed phenotypes of iRhom2 deficiency and cub deletion, as well as the pathologies associated
132 with the human TOC mutations, clearly point to a central role of iRhom2 in epidermal tissue. While
133 high iRhom2 expression is often primarily associated with immune cells, its expression pattern in the
134 epidermis is not yet well defined. Hence, we analysed gene expression data from skin biopsies of
135 healthy individuals obtained from publicly available microarray data (Hruz et al., 2008). We indeed
136 observed a robust expression of iRhom2 in the skin samples (Fig. 1C). Moreover, primary human
137 keratinocytes have significantly higher levels of iRhom2 expression compared to primary fibroblasts,

138 artery smooth muscle cells, and bronchial smooth muscle cells (Fig. 1C). Notably, the ratio of iRhom2
139 to iRhom1 is substantially higher in keratinocytes than in other primary cell types (Fig. 1C; Fig. S1A),
140 indicating a pivotal role for iRhom2 in regulating ADAM17 activity in keratinocytes *in vivo*. To verify the
141 microarray data, we analysed iRhom1 and iRhom2 protein levels via immunoblotting and gene
142 expression via RT-qPCR in primary keratinocytes and fibroblasts. Indeed, in agreement with the
143 microarray data, we found higher protein levels and gene expression of iRhom2 in keratinocytes
144 compared to fibroblasts (Fig. 1D,E). This expression pattern aligns with the predominantly skin-related
145 manifestations of TOC and cub. We found a similar pattern in murine primary keratinocytes, again
146 highlighting iRhom2's importance in regulating ADAM17 activity in the skin (Fig. S1B).

147 Considering the known induction of iRhom2 expression in response to proinflammatory stimuli
148 (Babendreyer et al., 2020, Giese et al., 2021), we investigated whether the observed iRhom2 expression
149 patterns in primary keratinocytes were due to pre-activation by proinflammatory conditions. We found
150 a significant increase in iRhom2 gene expression in primary keratinocytes 24 hours after treatment with
151 proinflammatory stimuli, while iRhom1 showed no such elevation (Fig. 1F). This finding supports that
152 the high iRhom2 expression in primary keratinocytes is likely the basal level under physiological
153 conditions which can be further increased under inflammatory conditions. Furthermore, the gene
154 expression pattern of untreated keratinocytes is also consistent with the basal iRhom2 and iRhom1
155 gene expression pattern in healthy human skin biopsies (Fig. 1C).

156 Since TOC mutations also pose an increased risk of developing OSCC, we examined iRhom2 expression
157 in OSCC samples and compared them to healthy oesophagus squamous tissue, as well as samples from
158 OAC and a premalignant condition, called Barrett's oesophagus. In OSCC samples, we observed a
159 significant upregulation of iRhom2, accompanied by a downregulation of iRhom1, compared to healthy
160 oesophagus squamous tissue (Fig. 1G). The ratio of iRhom2 to iRhom1 was four times higher in OSCC
161 samples than in the healthy tissue. While OAC samples also showed a significantly elevated iRhom2-
162 iRhom1 ratio, the increase was less pronounced (Fig. 1G). On the other hand, samples from Barrett's
163 oesophagus exhibited no change in the ratio but displayed an overall reduction in iRhom1 and iRhom2
164 gene expression. Furthermore, we found a significant upregulation of ADAM17 gene expression
165 exclusively in OSCC samples (Fig. S1C). In contrast, ADAM10, a close relative of ADAM17 with partially
166 overlapping substrate spectrum and independent of iRhom functions, did not show this expression
167 pattern (Fig. S1C). The gene expression of EGFR ligands, TGFα and AREG, crucial ADAM17 substrates,
168 did not show significant changes in OSCC compared to healthy tissue (Fig. S1C). To ensure that the
169 elevated levels of iRhom2 in OSCC were not due to persistent proinflammatory conditions or the
170 presence of tumour microenvironment-associated immune cells, we examined proinflammatory
171 markers and immune cell markers. We observed no significantly elevated gene expression of TNF or IL6
172 (Fig. S1C), and only minimal gene expression of CD14, suggesting the presence of some

173 monocytes/macrophages in the samples but not in sufficient quantities to explain the high iRhom2
174 levels in OSCC (Fig. S1D; Fig. S2A,B).

175 In summary, the gene expression patterns of iRhom2 and ADAM17 support the notion of an important
176 role for iRhom2-dependent ADAM17 activity in both skin and OSCC, which is consistent with the
177 pathological consequences of TOC single point mutations and cub deletion.

178

179 **The N-terminal tail represents a large intrinsically disordered part of iRhom2.**

180 To investigate the molecular mechanisms underlying the functions of the N-terminal tail of iRhom2, we
181 performed *in silico* structural studies. Our bioinformatic analyses predict that the N-terminal tail of
182 iRhom2 has a largely unstructured/intrinsically disordered nature (Fig. 2A), which is typical for protein-
183 protein interaction interfaces (Dyson, 2016, Arakawa et al., 2023). Using the A.I.-based AlphaFold2
184 algorithm, we predicted the structural makeup of the N-terminus, which revealed an overall low pLDDT
185 and PAE, again confirming a lack of higher structural regions (Fig. 2B-D). Some isolated secondary
186 structures were predicted, but the N-terminus seems to be primarily intrinsically disordered (Fig. 2A-
187 F), which is a hallmark to promote protein-protein interaction.

188 However, while the N-terminus seems to play a crucial role in regulating the iRhom-ADAM17 complex,
189 only a handful of direct interactors such as FRMD8, ERK2, and 14-3-3 proteins have been identified
190 (Fig. 1A)(Cavadas et al., 2017, Grieve et al., 2017, Künzel et al., 2018, Oikonomidi et al., 2018,
191 Schumacher et al., 2023). Using ANCHOR2, we have identified an additional region that is highly likely
192 to be an interface for protein-protein interactions (Fig. 2E). Strikingly, this region is highly conserved
193 and includes all known TOC mutation positions (Fig. 2E-F). In addition, R192 in the middle of this TOC
194 site was found to be methylated in human iRhom2 by three independent high-throughput proteomic
195 screens (Figure 2F)(Guo et al., 2014, Hornbeck et al., 2015). This further supports the TOC site as a
196 regulatory interaction site, as protein methylation is a hallmark of protein interaction sites.

197 Furthermore, our bioinformatic analysis of the N-terminus of iRhom2 also indicates the presence of a
198 nuclear localisation sequence (NLS), which is consistent with recent observations of its translocation to
199 the nucleus after cleavage by the signal peptidase complex (Fig. 2G)(Dulloo et al., 2022).

200 Overall, the N-terminal tail represents a large intrinsically disordered region that provides distinct hubs
201 for regulation and interaction. Furthermore, all known TOC mutations are part of a predicted protein-
202 protein interaction site.

203

204 **The TOC mutations and the cub deletion result in distinct molecular consequences for**
205 **mature ADAM17.**

206 To gain a comprehensive understanding of the regulatory system acting on the iRhom2-ADAM17
207 complex, it is important to understand the molecular similarities and differences between the TOC
208 single point mutations and cub deletions, as they exhibit a strikingly similar phenotype in mice (Hosur
209 et al., 2018b). While the TOC mutations affect a distinct region, the cub deletion affects a large part of
210 the N-terminal tail encompassing different known regulatory and interaction sites such as two
211 phosphorylation sites, the TOC region as well as the ERK2 binding site (Fig. 2G). The exact binding site
212 of the FRMD8 interaction is not yet known, but the approximate binding region was mapped before
213 (Fig. 2G)(Künzel et al., 2018, Oikonomidi et al., 2018). Hence, in contrast to TOC mutations the cub
214 deletion affects most likely more regulatory aspects. To further dissect the molecular regulations of
215 iRhom2 and its dysregulation, we designed an additional N-terminal deletion (nd197) that still contains
216 the FRMD8 binding region and therefore retains binding to endogenous FRMD8 (Fig. 2G,H). In contrast,
217 we could not detect FRMD8 binding for the cub deletion. We created two additional deletions (nd349
218 and nd370) with almost the entire N-terminus removed (Fig. 2G,H) to compare the effect of complete
219 loss of the N-terminal tail with the partial deletions. We also hypothesised that the TOC single point
220 mutations only gradually affect the function of the identified TOC site (Fig. 2E). Hence, we designed the
221 deletion ndTOC (Δ182-192) to remove most of the TOC site (Fig. 2E-F). As expected, binding to FRMD8
222 in iRhom2 is not altered by either the TOC point mutation (I186T) or the deletion of the TOC site
223 (ndTOC) compared to wt-iRhom2 (Fig. 2I).

224 The TOC mutations are autosomal dominant and the cub deletion leads to a phenotype already in
225 heterozygosity. To analyse the direct molecular effects of these iRhom2 variants on ADAM17 regulation
226 in combination with wt-iRhoms, we used HEK293 cells with endogenous iRhom1 and iRhom2 (Fig. S1E)
227 as an already established and widely used model system (Cavadas et al., 2017, Sieber et al., 2022,
228 Kahveci-Türköz et al., 2023), with epithelial morphology (Inada et al., 2016).

229 As iRhom levels are a rate limiting factor for forward transport and maturation of ADAM17, increased
230 expression of either human or murine wt-iRhom2 results in more mature ADAM17 (Fig. 3A-C), as
231 shown before (Düsterhöft et al., 2021, Kahveci-Türköz et al., 2023). Consequently, the amount of
232 mature ADAM17 on the cell surface is also elevated (Fig. 3D,E). In contrast, expression of the murine
233 iRhom2 cub deletion does not promote higher levels of mature ADAM17 (Fig. 3A). Furthermore, the
234 three deletions nd197, nd349 and nd370 showed also a significant decrease in mature ADAM17 levels
235 compared to wt-iRhom2 (Fig. 3B). We also observed a significant reduction in total ADAM17 levels in
236 cells expressing these deletions compared to wt-iRhom2 or the negative control (Fig. 3A,B). In line with
237 these findings the amount of mature ADAM17 on the surface was also lower in cells expressing the

238 deletions compared to both wt-iRhom2 and even control cells (Fig. 3D), although the deletion
239 constructs can be detected on the cell surface similarly to wt-iRhom2 (Fig. S3B). Notably, these effects
240 seem to be FRMD8 independent since nd197 still binds endogenous FRMD8 (Fig. 2H).

241 Expression of iRhom2 with a human TOC mutation (I186T) or a deletion of the TOC site (ndTOC) also
242 shows a reduced amount of mature ADAM17 compared to wt-iRhom2 (Fig. 3C). ndTOC seems to lead
243 to an even stronger reduction than the single point mutation, suggesting that the complete deletion of
244 the TOC site has a stronger effect than the single point mutation (Fig. 3C). However, in contrast to the
245 larger deletions (nd187, cub, nd349 and nd379), we did not observe a reduction in the total amount of
246 ADAM17 (Fig. 3C). Both iRhom2_I186T and ndTOC exhibit a cell surface presence similar to that of the
247 wt-iRhom2 (Fig. S3C). iRhom2_I186T leads to increased ADAM17 surface localisation compared to
248 control cells and the impact on surface ADAM17 levels is not significantly different to cells with wt-
249 iRhom2 expression (Fig. 3E). Remarkably, ndTOC expression results in significantly lower levels of
250 surface ADAM17 compared to wt-iRhom2 (Fig. 3E).

251 These findings demonstrate the importance of the cytosolic iRhom2 N-terminus in regulating ADAM17
252 functions. They highlight the differential effects of TOC mutations and the cub deletion on iRhom2
253 function and their substantial impact on ADAM17 maturation, surface localisation and overall protein
254 levels. Overall, these findings suggest that the decrease in ADAM17 levels and downregulation of
255 surface ADAM17 seen in the cub deletion and to a lesser extent in the TOC site mutants occur in a
256 FRMD8-independent way. Importantly, the deletion of the TOC site in ndTOC shows a more severe
257 molecular phenotype than the TOC single point mutations. This is consistent with single point
258 mutations only partially disrupting TOC site functions, whereas a larger deletion has a more severe
259 effect.

260

261 **The iRhom2 N-terminus differentially regulates ADAM17-mediated shedding.**

262 Our findings that cub and TOC mutations decreases levels of mature ADAM17 is in line with recent *in*
263 *vivo* and *ex vivo* results (Siggs et al., 2014, Rabinowitsch et al., 2023). However, these findings are
264 counterintuitive to the earlier reported elevated ADAM17 shedding activity (Brooke et al., 2014, Hosur
265 et al., 2017, Hosur et al., 2018a, Hosur et al., 2018b). To analyse the effect of the N-terminus on
266 ADAM17 activity, we investigated the constitutive shedding of the ADAM17 substrates TGFα, IL1R2 and
267 AREG in HEK293 cells. As reported earlier, we found significantly increased substrate release with
268 additional expression of wt-iRhom2 compared to control cells (Fig. 4A,B)(Düsterhöft et al., 2021,
269 Kahveci-Türköz et al., 2023). Surprisingly, despite lower surface ADAM17 levels (Fig. 3D), ADAM17-
270 mediated shedding was not adversely affected in cells with N-terminal deletions nd197, cub and nd349
271 compared to control cells (Fig. 4A,B). In fact, shedding efficiency in cells with these deletions was

272 generally higher compared to shedding in control cells and comparable to cells expressing wt-iRhom2.
273 The largest deletion nd370 had the lowest ADAM17-mediated shedding, but was still comparable to
274 control cells (Fig. 4A,B).

275 To further examine the effects of large N-terminal deletions in iRhom2 on ADAM17-mediated shedding,
276 we used iRhom1- and iRhom2-deficient mouse embryonic fibroblasts (MEFs)(Christova et al., 2013).
277 These cells lack production of mature ADAM17, resulting in an absence of ADAM17-mediated
278 shedding. However, reintroduction of wt-iRhom2 expression effectively restored ADAM17-mediated
279 shedding (Fig. 4C). Surprisingly, constitutive ADAM17-mediated shedding was also restored for the N-
280 terminal deletions (nd197, cub and nd349), despite barely detectable amounts of mature ADAM17
281 present (Fig. S3D). However, the shedding activity restored by the N-terminal deletions was
282 significantly lower compared to cells expressing wt-iRhom2 (Fig. 4C). Interestingly, the largest deletion
283 (nd370), which lacked the third phosphorylation site, showed no restored shedding activity, similar to
284 control cells (Fig. 2G; Fig. 4C). Furthermore, we assessed ADAM17-mediated shedding stimulated by
285 the phorbol ester PMA (phorbol 12-myristate 13-acetate). While cells expressing wt-iRhom2 showed a
286 significant increase in shedding, this effect was not observed with iRhom2 deletion mutants (Fig. 4C).
287 This aligns with previous reports indicating that stimulated shedding is primarily driven by
288 phosphorylation at the described phosphorylation sites 1 and 2 (Cavadas et al., 2017, Grieve et al.,
289 2017), which are absent in all deletions (Fig. 2G).

290 In HEK293 cells, we further investigated the effects of the TOC mutations on AREG shedding.
291 Interestingly, additional expression of human wt-iRhom2 did not significantly increase constitutive
292 AREG shedding (Fig. 4D). This is consistent with our previous findings that overexpression of human
293 iRhom2 promotes shedding to a lesser extent than that of its mouse counterpart (Kahveci-Türköz et al.,
294 2023). Remarkably, iRhom2 has 96% sequence similarity (92% identity) in human and mouse, except
295 for a large insertion at the beginning of the N-terminus of human iRhom2 isoform 1, which was used
296 in this study (Fig. S3A). The discrepancy in shedding efficiency may be attributed to this dissimilarity.

297 Importantly, expression of the TOC mutations significantly increased shedding activity (Fig. 4D),
298 consistent with previous observations (Blaydon et al., 2012, Maney et al., 2015). Strikingly, we observed
299 even higher shedding efficiency with the complete TOC site deletion ndTOC (Fig. 4D), again showing a
300 more severe molecular phenotype than the single point mutations. Moreover, as expected, iRhom2
301 with TOC site mutations still promote PMA-stimulated ADAM17 shedding activity in iRhom1- and
302 iRhom2-deficient MEFs (Fig. 4E). However, the stimulated shedding activity of the TOC site mutants is
303 slightly but significantly reduced compared to wt-iRhom2, which is in line with reduced levels of mature
304 ADAM17 (Fig. 3C,E; Fig. 4E).

305 In summary, our results show that the N-terminus differentially regulates constitutive and stimulated
306 shedding and that the cub deletion loses the ability to promote stimulated ADAM17 activity.
307 Importantly, both larger N-terminal deletions and TOC mutations appear to lead to a reduction in
308 mature ADAM17 levels with concurrent higher constitutive ADAM17 activity.

309

310 **N-terminal deletions of iRhom2 accelerate turn-over of mature ADAM17**

311 To gain better insight into the molecular phenotypes of N-terminal iRhom2 mutations, we sought to
312 understand the underlying mechanisms. The observed decrease in mature ADAM17 levels can be
313 attributed to either an impaired maturation process or accelerated turnover leading to increased
314 internalisation of ADAM17 and its lysosomal degradation (Fig. 5A). Previous studies have shown that
315 destabilisation of the iRhom-ADAM17 complex by FRMD8 loss leads to increased lysosomal
316 degradation (Künzel et al., 2018, Oikonomidi et al., 2018). However, the effect we observed is FRMD8
317 independent and has not been studied before. To investigate whether the FRMD8-independent effect
318 of nd197 is due to accelerated degradation, we used the lysosomal inhibitors NH_4Cl and bafilomycin.
319 The use of these inhibitors for 8 h and 16 h rescued the levels of mature ADAM17 (Fig. 5B,C). After
320 16 h, the levels of mature ADAM17 in HEK293 cells expressing the cub or nd197 deletion reached those
321 of cells expressing wt-iRhom2 (Fig. 5C), indicating a similar maturation efficiency. Therefore,
322 accelerated turnover is likely the cause of the low mature ADAM17 levels when the deletions are
323 expressed. This is consistent with the reduced total levels of ADAM17 in cells expressing the deletions,
324 as maturation is still occurring, which depletes the pool of immature ADAM17, but the mature ADAM17
325 is not stable due to accelerated lysosomal degradation.

326 To further analyse the impact of the iRhom2 N-terminus on the turnover kinetic of ADAM17, we
327 performed a cycloheximide-based pulse-chase experiment (Fig. 5A). We observed a rapid decrease in
328 immature ADAM17 levels after inhibition of biosynthesis, as the maturation process continued and
329 subsequently immature ADAM17 levels declined until presumably no iRhom is left in the ER (Fig. 5D).
330 The presence of wt-iRhom2 facilitated this effect, significantly enhancing the reduction due to
331 increased ADAM17 transport to the Golgi and subsequent maturation. We found that nd197 and cub
332 deletions had the same effect (Fig. 5D), indicating that maturation process remained unaffected by the
333 N-terminal deletions.

334 Furthermore, the levels of mature ADAM17 decreased more rapidly in cells expressing the deletion
335 than in control cells or cells expressing wt-iRhom2 (Fig. 5D) indicating accelerated degradation of
336 mature ADAM17 in the presence of N-terminal deletions.

337 For comparison, we next studied the influence of TOC mutations on ADAM17 stability. 8 h of
338 bafilomycin-mediated lysosomal inhibition rescued the levels of mature ADAM17 in cells expressing

339 the TOC mutant to the same level as cells with wt-human iRhoms (Figure S3E). This suggests that the
340 same amount of mature ADAM17 is generated in cells expressing TOC mutants or wt-human iRhom2.
341 Lysosomal degradation of mature ADAM17 is slightly higher in cells with TOC mutations than in cells
342 expressing wt-iRhom2, resulting in slightly lower levels of total mature ADAM17 and less mature
343 ADAM17 on the cell surface, as described above (Figure 3C,E). However, this slightly accelerated
344 degradation does not seem to be strong enough to detect significant differences with the
345 cycloheximide-based pulse-chase experiments (Figure S3F).

346 Taken together, these results demonstrate the regulatory role of the N-terminus in controlling the
347 stability and turnover kinetics of mature ADAM17, but not immature ADAM17. In addition, the effects
348 of larger deletions are more severe compared to mutations or deletions at the TOC site, suggesting that
349 the stability of mature ADAM17 is only slightly affected by the TOC site, but is more dependent on the
350 interplay of other sites in the iRhom2 N-terminus. As there is no difference between nd197 and cub,
351 this mechanism appears to be FRMD8 independent.

352

353 **The iRhom2 N-terminal tail is a key determinant for regulating ADAM17 binding**

354 The interaction between iRhom and ADAM17 is a crucial requirement for their stability. Although the
355 transmembrane regions and extracellular domains are known determinants of the binding between
356 iRhom and ADAM17 (Cavadas et al., 2017, Grieve et al., 2017, Li et al., 2017, Düsterhöft et al., 2021,
357 Kahveci-Türköz et al., 2023), we nevertheless wondered whether the N-terminus could play a role in
358 this interaction. By co-immunoprecipitation, we analysed the binding between ADAM17 and iRhom2.
359 In both HEK293 cells and iRhom1- and iRhom2-deficient MEFs, we observed a significant decrease in
360 binding between ADAM17 and all deletions tested (nd197, cub, nd349 and nd370) compared to wt-
361 iRhom2 (Fig. 6A,B). However, the overall decrease in cellular ADAM17 levels could distort the results.
362 To address this issue, we engineered iRhom2 variants fused to the ER retention sequence KDEL, which
363 inhibits ADAM17 transport, maturation, and subsequent accelerated turnover of the iRhom2-ADAM17
364 complex (Fig. S4A) (Düsterhöft et al., 2021). In fact, even in this setting, we found a significant reduction
365 in ADAM17 binding for iRhom2 deletions compared to wt-iRhom2 (Fig. 6C; Fig. S4B). Interestingly, we
366 detected an additional significant reduction in ADAM17 binding for deletions larger than nd197,
367 indicating multiple regions in the N-terminus that regulate ADAM17 binding (Fig. 6A,C). This
368 observation is consistent with co-immunoprecipitation experiments using lysosomal inhibitors, where
369 inhibition of lysosomal degradation significantly increased the observable intact iRhom2-ADAM17
370 complex with nd197, but not with cub deletion (Fig. S4C). Under lysosomal inhibition, the precipitated
371 complexes with nd197 and cub showed increased amounts of mature ADAM17 indicating more rapid

372 degradation when in complex with these deletions (Fig. 6D,E). Importantly, we did not observe a
373 reduction in binding efficiency of the TOC site mutants (Fig. 6F).

374 In summary, our results clearly demonstrate the crucial role of the N-terminus for the binding affinity
375 between iRhom2 and ADAM17, which in turn influences the cohesion and stability of the iRhom2-
376 ADAM17 complex. Remarkably, there appear to be two parallel mechanisms regulating the ADAM17
377 interaction via the N-terminus: a clearly FRMD8-independent mechanism and a potential FRMD8-
378 dependent mechanism. Importantly, this ADAM17 interaction function is lost in the larger cub deletion
379 but not when only the TOC site is disrupted (Fig. 7).

380

381 **The TOC site represents a phosphorylation independent 14-3-3 binding site**

382 Using AlphaFold Multimer complex modelling, we screened the TOC site for interaction with putative
383 iRhom2 binding partners that we and others had previously reported (Cavadas et al., 2017, Grieve et
384 al., 2017, Düsterhöft et al., 2021). Thereby we identified 14-3-3σ/stratifin (SFN) as a potential interactor
385 for the TOC site (Fig. 7A). To analyse the dynamic nature of the TOC-site-SFN complex, we performed
386 molecular dynamics simulations and sampled 150 conformations within the RMSD (root-mean-square
387 deviation) equilibrium (Fig. 7B). A contact map based on this conformational assembly revealed the
388 interacting residues between the TOC site and SFN (Fig. 7C,D). Specifically, I186 interacts with a
389 hydrophobic cleft in SFN, while D188 and R197 form salt bridges with SFN residues (Fig. 7D). P189
390 shows no direct interaction but appears to maintain a local structure important for overall binding with
391 SFN (Fig. 7D,E). Strikingly, D188 forms a salt bridge with R56 and R60 of SFN, which are part of the
392 region that normally facilitates interaction with phosphorylated serine residues of 14-3-3 clients. Thus,
393 D188 appears to mimic a phosphoserine residue, facilitating a phosphorylation-independent mode of
394 14-3-3 binding. The consequences of the pathological TOC mutations on the complex stability and
395 interaction energies were assessed and, as expected, showed a profound effect on the complex
396 integrity (Fig. 7E). Based on these findings, we investigated whether overexpressed SFN, which is
397 predominantly expressed in skin and undetectable at endogenous levels in HEK293 cells (Fig. 7F,G),
398 shows altered interaction efficiency between wt iRhom2 and the I186T TOC mutant. Indeed, using
399 coIPs, we found that the I186T TOC mutant showed reduced interaction with SFN compared to wt
400 iRhom2 (Fig. 7G). These data are in line with our *in silico* analysis and confirm the role of I186 within
401 TOC for efficient SFN binding. Using a pan-14-3-3 antibody, we also found that other 14-3-3 isoforms
402 expressed endogenously interact with the TOC site (Fig. 7G).

403 Overall, the TOC site serves as a phosphorylation-independent 14-3-3 binding site and this interaction
404 is disrupted by pathological TOC mutations.

405

Discussion

The iRhom2-ADAM17 sheddase complex is vital for both inflammatory signals (including TNFα release) and EGFR signalling (via growth factor release such as AREG and TGFα). iRhom2 is a key regulator for ADAM17's trafficking, maturation, activity, and stability. Understanding its regulation is crucial for the molecular biology of ADAM17-associated diseases and, consequently, for potential therapies targeting these pathologies. These include chronic inflammation and cancer pathologies, such as the autosomal dominant hereditary disorder Tylosis Oesophageal Carcinoma (TOC) (Blaydon et al., 2012, Düsterhöft et al., 2019). TOC is caused by mutations in the cytosolic N-terminus of iRhom2, resulting in increased ADAM17 activity, elevated growth factor release and increased EGFR signalling. Mice with the cub (curly-bare) deletion exhibit a similar phenotype to mice with TOC mutations, and both phenotypes can be rescued by knocking out amphiregulin (Hosur et al., 2017, Hosur et al., 2018b). This suggests a shared molecular mechanism between the large cub deletion and TOC single point mutations. However, studies on the cub deletion have yielded conflicting findings regarding whether it has a positive or negative effect on ADAM17 shedding activity (Hosur et al., 2014, Siggs et al., 2014, Maney et al., 2015, Grieve et al., 2017). In contrast, TOC mutations in iRhom2 clearly increase ADAM17-mediated shedding (Blaydon et al., 2012, Brooke et al., 2014), which is consistent with our results. In addition to TOC single point mutations, we used a complete deletion of the TOC site, resulting in an even more pronounced effect.

We identified the TOC site as a phosphorylation-independent 14-3-3 protein binding site that appears to have a restrictive effect on constitutive ADAM17 activity, which is disrupted by the pathological TOC mutations (Fig. 8). 14-3-3 proteins, as phosphoserine and phosphothreonine binding proteins, regulate most cellular processes. With widespread expression in tissues, they serve as universal scaffolds, influencing the structure and function of diverse protein targets in key cellular signalling pathways (Obsilova and Obsil, 2022). Although the majority of reported 14-3-3 binding motifs involve phosphorylation, there are a few non-canonical examples. In particular, the L**D**LA box in the exoenzyme S of *Pseudomonas aeruginosa* and the WL**D**LE motif in the artificial peptide R18 show high affinity to 14-3-3 proteins (Obsilova and Obsil, 2022). These motifs consistently feature an aspartate residue surrounded by hydrophobic residues, which bears a striking resemblance to the IV**D**PL motif found within the TOC site. Our finding is also consistent with previous results that the TOC site may also facilitate binding to keratin (Maruthappu et al., 2017). 14-3-3 proteins are known to interact with keratins (Ku et al., 2002) and may therefore act as an adapter between iRhom and keratins.

In contrast, the larger cub deletion, which includes the entire TOC site, has more molecular consequences (Fig. 8): 1) The loss of stimulated ADAM17 activity is consistent with the loss of N-terminal phosphorylation sites. 2) Large deletions of the N-terminus reduce the efficiency of iRhom-

440 ADAM17 interaction and accelerate ADAM17 degradation, resulting in reduced levels of mature
441 ADAM17 and reduced ADAM17 surface localisation.

442 Previously identified phosphorylation-dependent 14-3-3 binding to the iRhom N-terminus appears
443 necessary for stimulated shedding (Cavadas et al., 2017, Grieve et al., 2017)(Fig. 8). In contrast,
444 constitutive shedding may be attenuated by efficient 14-3-3 binding to the TOC site, which would be
445 consistent with previously reported ADAM17 hyperactivation (Blaydon et al., 2012, Maney et al., 2015,
446 Hosur et al., 2017). Both the cub deletion and the TOC single point mutations still show substantial
447 amounts of constitutive ADAM17 shedding activity. It is important to note that while the cub deletion
448 results in less ADAM17 activity being measured compared to wt iRhom2, it also results in a profound
449 reduction of mature ADAM17 on the cell surface. Taking this into account, the shedding activity per
450 ADAM17 molecule appears to be up-regulated, while the overall shedding activity at the cellular level
451 appears to be reduced.

452 Interestingly, the largest deletion we used, nd370, which is also missing a third key phosphorylation
453 site and putative 14-3-3 binding site (Fig. 2G)(Cavadas et al., 2017, Grieve et al., 2017), additionally
454 shows reduced constitutive shedding. Taken together, these suggest that there are distinct signalling
455 pathways which differentially regulate 14-3-3 binding and, in turn, constitutive and stimulated
456 ADAM17 activity. More studies are needed to dissect these complex mechanisms.

457 Notably, recent studies have also highlighted the critical role of the KRAS-ERK1/2 pathway in the
458 shedding activity of the iRhom2-ADAM17 complex (Cavadas et al., 2017, Grieve et al., 2017, Sieber et
459 al., 2022). KRAS-G12 mutants in tumour cells harbouring iRhom2 with TOC mutations further enhance
460 constitutive ADAM17-mediated shedding (Sieber et al., 2022). Interestingly, an ERK2 binding site was
461 recently identified within the N-terminus upstream of phosphorylation sites 1 and 2
462 (Fig. 2G)(Schumacher et al., 2023). Since this ERK2 interaction site is not present in cub, it appears to
463 be more relevant for stimulated shedding rather than constitutive shedding.

464 The N-terminus of iRhoms emerges as a critical determinant for the stability and activity of the iRhom-
465 ADAM17 complex. This is again supported by our data and was recently also confirmed *in vivo*: mice
466 with the cub mutation show decreased ADAM17 levels in different tissues (Rabinowitsch et al., 2023).
467 Recent findings highlight the significance of FRMD8-binding in regulating iRhom stability and,
468 consequently, ADAM17 stability and functions (Künzel et al., 2018, Oikonomidi et al., 2018). While the
469 loss of FRMD8 binding may contribute to the molecular consequences observed in cub deletions, our
470 observations demonstrate similar effects on mature ADAM17 stability in the nd197 deletion, which
471 retains the ability to bind FRMD8. This suggests that the N-terminus exerts a stabilising effect on the
472 iRhom-ADAM17 complex, largely independent of FRMD8: When these parts of the iRhom2 N-terminus,

473 which are not involved in FRMD8 binding, are deleted, accelerated turnover still occurs. Notably, TOC
474 mutants also show an effect on the stability of mature ADAM17, but to a lesser extent.

475 Our study reveals that not only the transmembrane helix 1 and the IRHD, as previously described (Li et
476 al., 2017, Tang et al., 2020, Düsterhöft et al., 2021, Kahveci-Türköz et al., 2023), but also the iRhom2
477 N-terminus, contributes to ADAM17 binding. Through our ER-trapping approach, we have
478 demonstrated that the reduced binding of ADAM17 is not attributable to decreased ADAM17 levels.
479 Notably, the anterior half of the N-terminus (nd197) emerges as particularly crucial for efficient
480 ADAM17 interaction. However, larger deletions like the cub deletion (Δ268) result in an additional
481 significant reduction in binding efficiency, potentially mediated by FRMD8.

482 We postulate that while the binding affinity to ADAM17 is significantly reduced, iRhom2 N-terminal
483 deletions such as cub retain the ability to bind immature ADAM17 in the ER, facilitating efficient
484 transport through the secretory pathway and normal maturation of ADAM17. During maturation, the
485 proteolytic removal of the ADAM17 prodomain may further decrease binding affinity, as our recent
486 study identified the prodomain as an additional binding determinant between the ADAM17
487 ectodomain and the IRHD (Kahveci-Türköz et al., 2023). The reduced cohesion of the iRhom2-
488 matureADAM17 complex on the cell surface appears to induce instability and accelerated turnover,
489 culminating in lysosomal degradation (Fig. 8).

490 In our study, we focused on the molecular functions of the iRhom2 N-terminus to unravel the intricate
491 regulatory system of the iRhom2-ADAM17 complex. It is important to note that our study did not
492 explore the integration of these mechanisms into a more complex *in vivo* system. Importantly,
493 ADAM17 activity at the cellular level *in vivo* is dependent on cell type-specific endogenous protein
494 levels of iRhom1, iRhom2 and ADAM17, which will also influence the manifestations of pathological
495 changes in the iRhom-ADAM17 axis (Rabinowitsch et al., 2023). Here it is also important to consider
496 that ADAM17 substrate specificity appears to be differentially regulated by iRhom1 and iRhom2
497 (Maretzky et al., 2013, Tang et al., 2020). In addition, iRhom functions independent of the ADAM17
498 pathway may also be involved in the manifestation of TOC and cub pathologies. For example, the N-
499 terminus of iRhom can be cleaved and translocated into the nucleus where it exerts incompletely
500 understood effects on gene expression (Dulloo et al., 2022, Zanotti et al., 2022). It is also critical to
501 recognise that altered ADAM17 activity can also initiate feedback loops that further modulate its own
502 activity, including the induction of ADAM17 activity by activation of the EGF receptor pathway (Grieve
503 et al., 2017, Kubo et al., 2022, Sieber et al., 2022) and induction of gene expression of ADAM17, iRhoms
504 and other regulators through various pathways including TNFα signalling (Arcidiacono et al., 2018,
505 Babendreyer et al., 2020, Giese et al., 2021, Kubo et al., 2022). In addition, exogenous stimuli and cell

506 stimulation, for example by LPS, also affect ADAM17 activity and gene expression of iRhom2, ADAM17
507 and its substrates (Arndt et al., 2011, McIlwain et al., 2012, Lu et al., 2017, Düsterhöft et al., 2021).

508 As the TOC mutations affect iRhom2, it is important to note that high iRhom2 expression is often
509 predominantly associated with immune cells and inflammatory conditions. This role of iRhom2
510 becomes apparent when considering that mice lacking iRhom2 have a seemingly healthy phenotype
511 but show impaired immune responses (Adrain et al., 2012, Christova et al., 2013, Issuree et al., 2013).
512 However, the high level of iRhom2 gene expression we observed in keratinocytes highlights the
513 important role of iRhom2 in skin homeostasis. This would be consistent with the TOC skin
514 hyperkeratosis phenotype and, in contrast, the reduced thickness of stress calluses in iRhom2 KO mice
515 described previously (Fig. 8)(Blaydon et al., 2012, Brooke et al., 2014, Maney et al., 2015, Maruthappu
516 et al., 2017). Notably, in patients with TOC mutations, tylosis manifests between the ages of 7 and
517 puberty, while cancer develops much later in life (Ellis et al., 2015), hinting at a cumulative effect over
518 time. This is in line with our finding that disruption of the TOC site leads to a gradual effect on iRhom2-
519 ADAM17 complex functions: The larger deletion of the TOC site has a stronger effect on ADAM17
520 activity than single point mutations.

521 Furthermore, we found a significant increase in iRhom2 and ADAM17 gene expression in oesophageal
522 squamous cell carcinoma (OSCC) compared to healthy oesophageal squamous tissue. This indicates
523 that the iRhom2-ADAM17 complex is a potential tumour marker for OSCC, which seems to be in line
524 with the fact that patients with TOC mutations, which increases ADAM17 activity, have a higher risk of
525 developing OSCC (Fig. 8).

526 Overall, our results shed new light on the regulation of the iRhom2-ADAM17 complex by the
527 N-terminal tail of iRhom2. The intrinsically disordered nature of the N-terminus makes it an extensive
528 hub for protein binding and regulation. The molecular functions highlighted in our study warrant
529 further analysis and could potentially serve as viable targets for modulating ADAM17 activity. They
530 could offer promising avenues for combating ADAM17-associated pathologies such as cancer or
531 chronic inflammation.

532

533

534 **Methods**

535

536 *Bioinformatics*

537 Multiple sequence alignments were generated by utilising Clustal Omega (Sievers et al., 2011).
538 Secondary structure prediction and analysis of intrinsically disordered regions were done with IUPred3
539 (Meszaros et al., 2009, Erdos et al., 2021), NetSurfP-2.0 (Klausen et al., 2019) and ANCHOR2 (Dosztanyi
540 et al., 2009, Meszaros et al., 2009, Meszaros et al., 2018). The following sequences were used
541 (UniProtKB entries): Q6PJF5 (human iRhom2) and Q80WQ6 (murine iRhom2). Nuclear localisation
542 sequence analysis was performed with NLStraddamus (Nguyen Ba et al., 2009).

543 To identify conserved sequence regions, the tool CONYAR (Conserved You Are) was employed to
544 perform high-throughput comparison of as many sequences of a target protein as possible (Kahveci-
545 Türköz et al., 2023).

546

547 *Structural modelling and molecular dynamics simulations*

548 *Ab initio* structure prediction of the cytosolic iRhom2 N-terminus was done with AlphaFold2 and
549 AlphaFold Multimer (Jumper et al., 2021) utilising ColabFold (Mirdita et al., 2022). Structural modelling
550 using the deep learning algorithm AlphaFold2 was done without homology templates. MMseq2 was
551 used as the multiple sequence alignment. Structural modelling was performed in 12 iterations.
552 ChimeraX was used to visualise the structures (Pettersen et al., 2021).

553 Molecular dynamics simulation was used to analyse the dynamics of the SFN-TOC-site complex over
554 time. The highest ranked AlphaFold model of the complex was used. The system was immersed in TIP3P
555 water in a cubic box with 1.0 nm padding and neutralised with 150 NaCl. The MD simulation was
556 performed using GROMACS2020.6 (Pronk et al., 2013) with the AMBER99SB-ILDN force field (Lindorff-
557 Larsen et al., 2010). The system was first energy minimised. Equilibration MD simulations were
558 performed with periodic boundary conditions. The temperature was equilibrated using an NVT
559 ensemble for 1 ns followed by an NPT ensemble for 1 ns to equilibrate the pressure using the v-rescale
560 temperature and Parrinello−Rahman pressure coupling method during production. Finally, the
561 production MD simulations were performed for 100 ns (300 K and 1 atm). Between 85 ns and 100 ns,
562 which was within RMSD equilibrium, 150 conformations/frames were sampled (Δt = 100 ps). Biopython
563 (Cock et al., 2009) was used to calculate the distances between Cα within this conformational
564 compilation of each frame and to generate a temporal contact map (cutoff <12 Å) with the frequency
565 of contacts within the sampled 15 ns. FoldX (v5) PSSM and Position Scan (Van Durme et al., 2011) were

566 used to analyse the influence of single point mutations in the sampled conformations on binding and
567 overall stability, respectively.

568

569 *In silico gene expression analysis*

570 We accessed Affymetrix Human Genome U133 Plus 2.0 Array platform data from public repositories,
571 curated by the GENEVESTIGATOR platform (Immunai, USA)(Hruz et al., 2008). The GENEVESTIGATOR
572 software was utilised for gene expression meta-analysis of indicated genes in various tissues, biopsies,
573 and primary cells (assessed on 20 May 2023). To analyse gene expression patterns under physiological
574 conditions, only samples from healthy and untreated tissues were included. Similarly, for assessing
575 baseline gene expression in cancerous tissue, only untreated samples were considered.

576 List of used experiment IDs for indicated tissue and primary cells: a) murine heart: MM-00170 (Muchir
577 et al., 2007), MM-00253 (Dufour et al., 2007), MM-00257 (Zhao et al., 2007), MM-00262 (Alcendor et
578 al., 2007), MM-00300 (Ramchandran et al., 2006), MM-00322, (Thorrez et al., 2008), MM-00330 (Lattin
579 et al., 2008), MM-00368 (Barger et al., 2008), MM-00384 (Wong et al., 2010), MM-00476 (Abd Alla et
580 al., 2016), MM-00485 (Oka et al., 2011), MM-00492 (Wang et al., 2016), MM-00497 (Shuai et al., 2011),
581 MM-00507 (Shuai et al., 2011), MM-00561 (Ricard et al., 2010), MM-00834 (Traister et al., 2013), MM-
582 00841 (Mercader et al., 2012), MM-01538 (Gambino et al., 2013), MM-01642 (Lucas et al., 2014), MM-
583 01875 (Lucas et al., 2014); b) murine primary fibroblast (dermis): MM-00159 (Vallender and Lahn,
584 2006), MM-00180 (Vallender and Lahn, 2006), MM-00627 (Garinis et al., 2009), MM-00724 (Garinis et
585 al., 2009); c) murine primary keratinocytes: MM-01215 (Allende et al., 2013); d) healthy human
586 epidermis tissue (biopsy): HS-02924 (Esaki et al., 2015); e) human primary keratinocytes (untreated):
587 HS-02625 (Yunoki et al., 2018), HS-02787 (Busch et al., 2008), HS-02490 (Swindell et al., 2012), HS-
588 00220 (Sa et al., 2007); f) human primary keratinocytes (treated with TNFα, IFNα, IFNγ or IL4; 24 h):
589 HS-02490 (Swindell et al., 2012); g) human primary keratinocytes (treated with 10 ng/ml I IFNγ; 96 h):
590 HS-02625 (Yunoki et al., 2018); h) human primary fibroblasts (untreated): HS-00393, HS-00481 (Chen
591 et al., 2008), HS-00805 (Verkerk et al., 2009), HS-00928 (Wang et al., 2012), HS-00963, HS-00989
592 (Strunnikova et al., 2009), HS-01109 (Visser et al., 2012), HS-01279 (Marchina et al., 2014), HS-01311
593 (Henrichsen et al., 2011), HS-01326 (Voets et al., 2012), HS-02421 (Smith et al., 2008); i) primary artery
594 smooth muscle cells (heart): HS-00478 (Shalhoub et al., 2010); j) primary bronchial smooth muscle
595 cells: HS-00039 (Bosse et al., 2007); k) healthy oesophagus squamous tissue (biopsy): HS-01298 (Wang
596 et al., 2013), HS-00217, HS-00017 (Roth et al., 2006), HS-01525 (Sato et al., 2013); squamous cell
597 carcinoma (grade G1): HS-01298 (Wang et al., 2013); oesophagus adenocarcinoma: HS-00002; HS-
598 01298 (Wang et al., 2013); Barrett´s oesophagus (pre-malignant): HS-01298 (Wang et al., 2013);

599 primary macrophages: HS-01265; primary granulocytes: HS-00250; primary leukocytes: HS-00261;
600 primary monocytes: HS-01403.

601

602 *Cloning*

603 The cloning procedures were performed as previously described (Düsterhöft et al., 2021): NEBuilder
604 HiFi DNA Assembly Master Mix (NEB, E2621L) was utilised to produce different plasmids with the
605 desired inserts according to the manufacturer's instructions. All iRhom constructs were cloned into the
606 pMOWS backbone (Ketteler et al., 2002, Düsterhöft et al., 2021). Site-directed mutagenesis was
607 performed using overlapping PCR (Ho et al., 1989).

608

609 *Cell culture*

610 All cells were cultured in a humidified incubator at 37 °C, 5% CO_2 in DMEM10% (unless otherwise
611 indicated). DMEM10% consists of DMEM high-glucose (Sigma-Aldrich) supplemented with 10% foetal
612 calf serum (PanBiotech), 100 mg/l streptomycin (Sigma-Aldrich) and 60 mg/l penicillin (Sigma-Aldrich).
613 Production of stable cell lines was done as described before (Düsterhöft et al., 2021). MEFs double
614 deficient for iRhom1 and iRhom2 were obtained from indicated mouse lines as described before
615 (Christova et al., 2013, Düsterhöft et al., 2021). HEK293 cells were purchased from German Collection
616 of Microorganisms and Cell Cultures (GmbH DSMZ- No. ACC 305). Normal human epidermal
617 keratinocytes and human dermal fibroblasts were isolated from human skin samples as described
618 before (Schmitt et al., 2018). Primary keratinocytes were cultivated in Dermalife K – Life Line (Cell
619 Systems LL-0007). Primary fibroblasts were cultivated in DMEM10%.

620

621 *Quantitative PCR (RT-qPCR)*

622 mRNA expression levels were measured by quantitative PCR and normalised to the mRNA expression
623 levels of the selected reference genes. Cytochrome c1 (CYC1) and ribosomal protein L13a (RPL13A)
624 were chosen as the most stable reference genes based on the results from the CFX Maestro Software
625 1.1 (Bio-Rad). RNA was extracted using RNeasy Kit (Qiagen) and quantified photometrically (NanoDrop,
626 Peqlab, Erlangen, Germany). For reverse transcription, the PrimeScriptTM RT Reagent Kit (Takara Bio
627 Europe) was used, according to the manufacturer's protocol. PCR reactions were performed in
628 duplicates of 10 µl volume comprising 1 µl of cDNA template, 5 µl iTaq Universal SYBR Green Supermix
629 (Bio-Rad), 3 µl H_2O and 0.5 µl forward and reverse primer. The following primers were used with the
630 primer annealing time given in brackets: CYC1 (forward: AGC TAT CCG TGG TCT CAC C, reverse: CCG CAT
631 GAA CAT CTC CCC ATC; 59 °C), RHBDF1 (forward: GAC AGC CCA CAT CTC TTC AC , reverse: TCC TTG CTC

632 ACT CCA AAC CA; 56 °C), RHBDF2 (forward: CGA TTG ACC TGA TCC ACC, reverse: CAA AGT CTC CGA GCA
633 GTC C; 58 °C) and RPL13A (forward: GCC CTA CGA CAA GAA AAG CG, reverse: TAC TTC CAG CCA ACC
634 TCG TGA; 60 °C). All RT-qPCR reactions were performed on a CFX Connect Real-Time PCR Detection
635 System (Bio-Rad) using the following protocol: 40 cycles of 10 s denaturation at 95 °C, followed by 10 s
636 annealing at the corresponding temperatures and 15 s amplification at 72 °C. PCR efficiency was
637 calculated from the uncorrected RFU values using LinRegPCR version 2020.0 (Ruijter et al., 2009). CFX
638 Maestro Software 1.1 (Bio-Rad) was used for relative quantification.

639

640 *Co-immunoprecipitation and enrichment of glycosylated proteins*

641 Precipitation experiments were done as described before (Düsterhöft et al., 2021, Kahveci-Türköz et
642 al., 2023): Cells were lysed in 1 ml lysis buffer (50 mM Tris, 2 mM $CaCl_2$, 137 mM NaCl, 2 mM EDTA,
643 10 mM 1,10-Phenanthroline, pH 7.5) supplemented with cOmplete™ protease inhibitor (Sigma;
644 11697498001). The lysates were cleared by centrifugation at 16,000 x g for 20 minutes at 4 °C. For the
645 enrichment of glycosylated proteins, 450 µl of cleared lysate was incubated with 30 µl of Concanavalin
646 A sepharose (Sigma; C9017). For co-immunoprecipitations (coIPs), 450 µl of cleared lysate was
647 incubated with 10 µl of anti-HA magnetic beads (Thermo; 88836). The lysates were incubated with the
648 beads for 90 min. Afterwards, the beads were washed five times with lysis buffer. The beads were
649 heated in 40 µl reducing loading buffer (3% SDS, 16% glycerol, 8% 2-mercaptoethanol, 0.01%
650 bromophenol blue, 0.1 M Tris HCl, pH 6.8) at 65 °C for 20 minutes.

651

652 *Western blotting*

653 Samples were subjected to SDS-PAGE and transferred onto PVDF membranes (Millipore, Immobilon-
654 FL). Membranes were blocked with 5% non-fat dry milk in TBS (50 mM Tris, 150 mM NaCl, pH 7.4) for
655 20 min at room temperature. Primary antibodies were incubated overnight at 4 °C in 0.1% Tween-TBS
656 and 1% BSA. After three washes with 0.1% Tween-TBS, membranes were incubated with secondary
657 antibody for 1 h at room temperature. Additional washing steps included one wash with 0.1% Tween-
658 TBS and three washes with TBS. Protein detection was performed using the Odyssey 9120 imager
659 system (LI-COR) and the ChemiDoc MP Imaging System (Bio-Rad). Band intensities were quantified
660 using Image Studio Lite software (LI-COR). The following primary antibodies were used: αADAM17
661 (1:1000; Abcam; ab39162), αHA (1:2000; Biolegend; 901502), αTransferrin-receptor (1:2000; Thermo,
662 H68.4, 13-6800), αGAPDH (1:2000; Thermo, GA1R, 15738), αiRhom2 (1:1000; R&D; 996308;
663 MAB10048), α14-3-3sigma (1:5000, Sigma, #PLA0201), α14-3-3pan (1:1000, Cell Signaling Technology,
664 #8312S). The following secondary antibodies were used at the indicated dilutions: DyLight-680-
665 conjugated αmouse (1:20000; Thermo; 35519), DyLight-800-conjugated αrabbit (1:20000; Thermo;

666 35571), HRP-conjugated goat αmouse and αrabbit (1:20000; Jackson ImmunoResearch Laboratories,
667 Inc).

668

669 *Shedding activity - AP-Assay*

670 ADAM17-mediated shedding activity was measured by an alkaline phosphatase (AP)–based assay as
671 described before (Düsterhöft et al., 2021, Kahveci-Türköz et al., 2023). In brief, we used cells transfected
672 with ADAM17 substrates fused to an alkaline phosphatase to analyse shedding activity: The following
673 ADAM17 substrates cloned in pCndA3.1 were utilised: AP-IL1R2, AP-TNFα, AP-AREG. HEK293 cells
674 stably expressing the indicated iRhom2 constructs were transiently transfected with the indicated
675 substrate. In the case of MEFs, the indicated iRhom2 construct combined with the indicated substrate
676 was transiently transfected. Shedding activity was assessed under different conditions: either the
677 metalloprotease inhibitors marimastat (broad-spectrum, 10 µM) (Sigma; M2699) or TAPI1 (ADAM17
678 preferential inhibitor, 10 µM) (Sigma; SML0739) were used. When indicated, cells were stimulated with
679 100 nM PMA (Sigma; P1585). DMSO served as the vehicle control. Following treatment, cells were
680 incubated: 90 min (AREG, TGFα), 120 min (IL1R2), or 240 min (AREG) at 37 °C. To evaluate proteolytic
681 activity of ADAM17, we measured alkaline phosphatase (AP) activity in both the supernatant and cell
682 lysates (lysis buffer: 50 mM Tris, 137 mM NaCl, 2 mM EDTA, 10 mM 1,10-phenanthroline, pH 7.5,
683 supplemented with cOmplete™ protease inhibitor). By continuously measuring AP activity at 405 nm
684 using the FLUOstar Optima (BMG LABTECH) after adding a p-nitrophenyl phosphate (PNPP) solution
685 (Thermo; 37620), we calculated the slope representing the change in absorbance at 405 nm per min.
686 ADAM17 activity was determined by calculating the PNPP substrate turnover (AP activity) in the
687 supernatant relative to the total turnover in the supernatant plus cell lysate.

688

689 *Flow cytometric analysis*

690 The staining process was conducted using PBS with 0.2% BSA as the assay buffer, and all steps were
691 carried out at 4 °C or on ice. A total of $2x10^5$ cells of interest were incubated with the primary antibody
692 for 1 h. Subsequently, cells were washed twice with 400 µl of assay buffer. The secondary antibody was
693 added, and cells were incubated in the dark for 45 mins. Following two additional washing steps, the
694 fluorescence signal was assessed using flow cytometry (LSRFortessa, BD Biosciences, Heidelberg,
695 Germany), and FlowJo V10 software was employed for data analysis. The geometric mean of
696 fluorescence intensity was determined to assess cell surface localisation. The primary antibodies used,
697 along with their dilutions, were as follows: αADAM17 (1:100; R&D Systems; MAB 9301), αHA (1:500;
698 Biolegend; 901502). The secondary antibody used was Allophycocyanin-conjugated αmouse (1:200;
699 Jackson ImmunoResearch; 115-135-164).

Lysosomal inhibition

Cell cultures were first grown to approximately 80% confluence. Cells were treated with either bafilomycin A1 (B) or NH_4Cl (N). An untreated control was also included using DMSO as a vehicle control. The cells were then incubated for 8 h (B: 0.1 µM; N: 20 mM) or 16 h (B: 0.5 µM; N: 40 mM). After incubation, the plates were placed on ice and the medium was discarded. The cells were washed once with PBS and then harvested with 1 ml cold PBS. A 10 µl aliquot was taken from the cell suspension to determine the number of cells for sample adjustment. The harvested cells were centrifuged at 1000 g for 5 min at 4°C and the supernatant was discarded. Cell pellets were used for lysis and coIPs followed by Western blotting as described above.

Cycloheximide-based pulse chase experiment

Cell cultures were used at approximately 80% confluence. Cells were incubated with cycloheximide (10 µg/ml) for 3 or 6 h. After washing with PBS, the cells were harvested in 1 ml cold PBS and a 10 µl aliquot was taken from the cell suspension to determine the number of cells for sample adjustment. Harvested cells were pelleted and used for lysis followed by Western blotting as described above.

Statistics

Statistic was done as described before (Düsterhöft et al., 2021): Experiments were repeated at least three times, as indicated in the figure legends. Quantitative data are presented as mean with standard deviation (SD). Statistical analysis was performed using the generalised mixed model analysis (PROC GLIMMIX, SAS 9.4, SAS Institute Inc., Cary, North Carolina, USA), assuming normal, lognormal, or beta distribution, with the day of the experiment considered as a random factor to assess treatment effect differences across the results. Diagnostic tests, including residual analysis and the Shapiro-Wilk test, were utilized. In cases of heteroscedasticity (as determined by the covtest statement), degrees of freedom were adjusted using the Kenward-Roger approximation. All p-values were adjusted for multiple comparisons using the false discovery rate (FDR). Statistical significance was defined as $p < 0.05$, with the following notation: p: * < 0.05, ** < 0.01, *** < 0.001.

Declarations

Ethics approval

732 This study was conducted according to the principles of the Declaration of Helsinki and approved by
733 the ethics committee of the Medical Faculty RWTH Aachen, Germany (EK 188/14).
734
735 **Authors' contribution**
736 S.D. conceived, designed, and coordinated the study and wrote the manuscript. S.D. and A.L. analysed
737 data and revised the manuscript. S.D., K.B., L.L., S.K.T., C.F., F.S., S.K., D.K., C.G, N.T. and X.G. performed
738 experiments and analysed the results. S.D. conducted protein bioinformatics analysis, structure
739 prediction and MD simulations. A.B. developed the algorithm for high-throughput identification of
740 conserved regions and performed conservation analysis. S.D. and S.K. performed meta-analysis of *in*
741 *vivo* and *ex vivo* datasets. C.A. generated FRMD8/iTAP knock-out cells. S.H. and J.M.B. isolated primary
742 keratinocytes and fibroblasts. All authors read and approved the final version of the manuscript.
743
744 **Funding**
745 To S.D. Research Fellowship of the German Research Foundation (280679981), ERS Start-up
746 (StUpPD_299-18) and two START grants (#691903-06/19 and #692305- 06/23) of the Medical Faculty
747 of the RWTH Aachen University. To A.L. funding from the German Research Foundation (418426903)
748 and from the Interdisciplinary Centre for Clinical Research (IZKF) Aachen (A-1-5).
749
750 **Conflict of interests**
751 The authors have no relevant financial or non-financial interests to disclose.
752
753 **Abbreviations**
754 a disintegrin and metalloproteinases (ADAM); amphiregulin (AREG); co-Immunoprecipitation (coIP);
755 epidermal growth factor receptor (EGFR); FRMD8 (FERM Domain Containing 8), interferon (IFN);
756 interleukin (IL); interleukin 1 receptor 2 (IL1R2); iRhom homology domain (IRHD); oesophageal cancer
757 (OC); oesophageal adenocarcinoma (OAC); oesophageal squamous cell carcinoma (OSCC); predicted
758 aligned error (PAE); predicted local distance difference test (pLDDT); transforming growth factor alpha
759 (TGFα); tumour necrosis factor alpha (TNFα)
760
761 **Acknowledgment**
762 We thank Johanna Jakob for cultivation of the primary cells.
763

764 **Figure legends**

765 **Figure 1:iRhom2 gene expression is high in skin and OSCC (A)** Structurally, iRhoms have a distinct
766 topology composed of a rhomboid core with seven transmembrane helices (TMH). The extracellular
767 iRhom homology domain (IRHD) is situated between TMH1 and TMH2. Additionally, iRhoms possess a
768 large cytosolic N-terminal tail: 375 residues in murine iRhom2 and 403 residues in human iRhom2.
769 Relative positions of key characteristics are labelled for murine iRhom2: (1) putative FRMD8 binding
770 site; (2) TOC mutation site - in human iRhom2: I186T (murine position: 156)(Blaydon et al., 2012),
771 D188N (murine position: 158)(Blaydon et al., 2012), D188Y (murine position: 158)(Mokoena et al.,
772 2018), P189L (murine position: 159)(Blaydon et al., 2012), R197S (murine position: 167)(Qu et al.,
773 2019); (3) phosphorylation sites and putative 14-3-3 binding sites. **(B)** Role of iRhoms in ADAM17
774 biology: iRhoms regulate ADAM17 by binding to immature proADAM17 in the ER and transporting it
775 to the Golgi for maturation. The inhibitory prodomain is then proteolytically removed by furin-like
776 proteases. This process allows mature ADAM17 in complex with iRhoms to localise to the cell surface
777 and initiate shedding of its substrates, enabling various pathways including TNFα and EGFR signalling.
778 **(C)** Curated Affymetrix Human Genome U133 Plus 2.0 Array platform data from public repositories
779 (Hruz et al., 2008) were assessed with the GENEVESTIGATOR software. The GENEVESTIGATOR platform
780 allows for the comparison of mRNA expression of genes between samples of different experimental
781 data sets: Gene expression levels of iRhom1 (RHBDF1) and iRhom2 (RHBDF2) from healthy human
782 epidermis tissue (n = 10), untreated primary human keratinocytes from healthy tissue (n = 13),
783 untreated primary human fibroblasts from healthy dermis tissue (n = 57), untreated primary human
784 artery smooth muscle cells from healthy heart tissue (n = 10), untreated primary human bronchial
785 smooth muscle cells from healthy heart tissue (n = 10) were analysed. To compare the gene expression
786 levels of iRhom1 and iRhom2 in one sample, the iRhom2/iRhom1 ratio was calculate for each sample.
787 **(D)** Immunoblot of cell lysates from primary keratinocytes or primary fibroblasts. n = 3. **(E)** RT-qPCR of
788 primary keratinocytes and primary fibroblasts. n = 3. **(F-G)** Data from curated Affymetrix Human
789 Genome U133 Plus 2.0 Array platform data as described in (C): **(F)** Gene expression levels of iRhom1
790 and iRhom2 in primary keratinocytes from healthy tissue treated with: untreated control (n = 13) or
791 treated for 24 h with indicated proinflammatory stimulants (n = 3) or treated for 96 h with IFNγ (n = 2).
792 **(G)** Gene expression levels of iRhom1 and iRhom2 in healthy human oesophagus squamous tissue
793 (n = 23) compared to expression levels in human oesophageal squamous cell carcinoma (OSCC; n = 8),
794 human oesophageal adenocarcinoma (OAC; n = 26) and Barrett´s oesophagus (n = 17).

795

796 **Figure 2: The cytosolic N-terminal tail of iRhom2 is an intrinsic disordered hub for regulation and**
797 **differentially controls levels of mature ADAM17. (A)** Using IUPred3 (Meszaros et al., 2009, Erdos et

798 al., 2021) and NetSurfP-2.0 (Klausen et al., 2019) , we assessed the probability of disordered regions
799 and the presence of different structural elements in the cytosolic N-terminus of murine and human
800 iRhom2 (residue 1 to 375). IUPred3 score describes the probability of disordered regions. NetSurfP-2.0
801 output gives the probability of the presence of disorder, alpha-helices, and beta-sheets. **(B)** *Ab initio*
802 structural modelling of the N-terminus of murine iRhom2 using the deep learning algorithm
803 AlphaFold2. Best ranked model is depicted in cartoon representation coloured according to pLDDT
804 (predicted local distance difference test in [%]) score. **(C)** Consistent with (A), the structural prediction
805 of the N-terminus of murine and human iRhom2 using AlphaFold2 demonstrates only small locally
806 structured regions: Hence the iRhom2 N-terminus is largely disordered, as indicated by the overall low
807 average pLDDT score per sequence position of the five predicted, ranked models. **(D)** The predicted
808 align error (PAE) of the best ranked structural models support this finding: the individual amino acid
809 residues in the disordered/unstructured N-terminus are largely not fixed in their position relative to
810 each other and therefore have a high spatial uncertainty (20 - 30 Å). **(E)** Using the bioinformatic tools
811 IUPred3 and ANCHOR2 (Mészáros et al. 2009) putative binding sites within the cytoplasmic N-terminus
812 of human iRhom2 were identified. The plots show the calculated probability for an amino acid residue
813 to be part of a binding site. Regions above 50% probability (ANCHOR2) and with a certain length are
814 putative binding sites such as the highly conserved region which harbours all known TOC mutations.
815 Our designed TOC site deletion ndTOC comprises the three main TOC mutations, but not the newest
816 identified R197S (Qu et al., 2019). **(F)** We used the algorithm CONYAR (Kahveci-Türköz et al., 2023) to
817 retrieve all available amino acid sequences of iRhom1 and iRhom2 from UniProtKB and compare them
818 to identify highly conserved regions within the amino acid sequences of that gene. In the case of
819 iRhom2 (query: RHBDF2) sequences from 381 species and in case of iRhom1 (query: RHBDF1)
820 sequences of 301 species were extracted. The TOC site was identified by CONYAR as a highly conserved
821 region and its conservation is shown as WebLogo representation. Asterisks indicate the positions of the
822 natural occurring TOC mutations in human iRhom2. M indicates the position of arginine methylation
823 found by high throughput proteomics (Hornbeck et al., 2015). **(G)** Overview of the relative position of
824 key regulatory sites and binding interfaces in wt-iRhom2 and in our designed N-terminal deletions.
825 Phosphorylation sites (P1, P2 and P3) are binding sites for 14-3-3 proteins. NLS: predicted nuclear
826 localisation sequence. **(H,I)** To analyse binding between iRhom2 constructs and endogenous FRMD8,
827 coIPs were performed using the indicated iRhom2 constructs (with HA tag) as bait. HEK293 cells stably
828 expressing the indicated murine iRhom2 deletions (H) or human iRhom2 constructs (I) as well as GFP
829 (ctr.) as negative control were used. At around 55 kDa the shorter fragment of cleaved iRhom2 (siR2)
830 as reported before (Adrain et al., 2012, Christova et al., 2013) is visible. This fragment was described
831 as consequence of cleavage by signal peptidase complex (Dulloo et al., 2022, Zanotti et al., 2022) but

832 may additionally occur as artefact after lysis as we detect inconsistent amounts of the small fragment
833 in different experiments. n = 4.

834

835 **Figure 3: The iRhom2 N-terminus regulates levels of mature ADAM17. (A)-(C)** Immunoblot of samples
836 from HEK293 cells stably expressing the indicated murine iRhom2 variants (A,B) or human iRhom2
837 variants (C) as well as GFP (ctr.) as negative control. Glycosylated proteins from cell lysates were
838 enriched with concanavalin A beads. HEK293 cells have endogenous iRhoms and therefore exhibit a
839 basal level of ADAM17 maturation. The maturation level of ADAM17 can be detected by the presence
840 of mature ADAM17 with lower molecular weight than immature ADAM17 (imA17). ADAM17
841 maturation was assessed by densitometric measurements and calculation of the ratio between mature
842 ADAM17 and immature ADAM17. Total ADAM17 levels were assessed by densitometric
843 measurements and calculation of the ratio between total ADAM17 (mature plus immature ADAM17)
844 divided by the respective input control. Values were normalised to the respective wt-iRhom2 sample.
845 n > 4. **(D)-(E)** Levels of surface ADAM17 in cells stably expressing indicated murine iRhom2 constructs
846 (D) or human iRhom2 constructs (E) were measured by flow cytometry. For quantification, the
847 geometric mean of the specific fluorescence signal was determined and normalised to the respective
848 wt-iRhom2. n > 4.

849

850 **Figure 4: N-terminal mutations in iRhom2 dysregulate ADAM17-mediated shedding. (A-E)**
851 Constitutive ADAM17-mediated shedding activity was assessed by performing an alkaline phosphatase
852 (AP) assay in HEK293 cells (A,B,D) and MEFs deficient for iRhom1 and iRhom2 (C,E) expressing the
853 indicated iRhom2 constructs. The ADAM17 substrate TGFα, IL1R2 or AREG tagged with AP were used.
854 The metalloprotease inhibitors marimastat (10 µM) or the more ADAM17 specific inhibitor TAPI1
855 (10 µM) were used as negative control. Where indicated, ADAM17 activity was additionally stimulated
856 by the phorbol ester PMA (100 nM). n > 4.

857

858 **Figure 5: The N-terminal tail of iRhom2 regulates protein turn-over kinetics. (A)** After biosynthesis in
859 the ER, ADAM17 is transported to the Golgi for maturation with the help of iRhoms. The complex of
860 mature ADAM17 and iRhom is transported to the cell surface. After internalisation, the complex is
861 degraded in the lysosomes. Like all ER proteins, to a certain extent immature ADAM17 can be
862 transported directly to the lysosome by ER-phagy. **(B-C)** To analyse the fate of mature ADAM17 in cells
863 expressing the nd197 and cub deletion, cells were treated with either NH_4Cl ("N") or bafilomycin ("B")
864 for 8 h (B) or 16 h (C) to inhibit lysosomal degradation. Levels of mature ADAM17 were assessed by
865 densitometric measurements and calculation of the ratio between mature ADAM17 and the loading

control GAPDH, which is independent of lysosomal degradation. (n = 4) **(D)** To assess the turn-over rate of ADAM17 a cycloheximide-based (Chx) pulse-chase experiment was performed. Reduction of ADAM17 levels was assessed by densitometric measurements and normalisation to 0 h Chx treatment (set to 1). (n = 3).

Figure 6: The N-terminus of iRhom2 regulates ADAM17 interaction. To analyse interaction between ADAM17 and the indicated iRhom2 variants, coIPs were performed using the iRhom variants (with HA tag) as bait. Immunoblotting and subsequent densitometric measurements were used to quantitatively analyse iRhom2-ADAM17 binding (ratio of co-precipitated ADAM17 and precipitated iRhom2) and normalised to wt-iRhom2. **(A)** HEK293 stably expressing indicated iRhom2 variants or GFP (ctr.) were used (n > 17). **(B)** MEFs from mice deficient for iRhom1 and iRhom2 stably expressing indicated iRhom2 variants or GFP (ctr.) were used (n = 4). **(C)** HEK293 expressing indicated iRhom2 variants or GFP (ctr.) fused to the ER-retention motif KDEL were used (n > 5). **(D) – (E)** To analyse the fate of mature ADAM17 specifically in the iRhom2-matureADAM17 complex containing either the nd197 deletion, cub deletion or wt-iRhom2, cells were treated with either 40 mM NH4Cl (N) or 500 nM bafilomycin (B) for 8 h or 16 h to inhibit lysosomal degradation. Maturation levels of bound ADAM17 was assessed by densitometric measurements and calculation of the ratio between mature ADAM17 and immature ADAM17. The quantitative analysis of ADAM17 binding can be found in Fig. S4C. (n = 4). **(F)** HEK293 stably expressing indicated human iRhom2 variants or GFP (ctr.) were used for coIP experiments as describe above. (n > 4).

Figure 7: The TOC site binds 14-3-3 proteins in a phosphorylation-independent manner. (A) The complex consisting of the TOC site peptide (P184 to R197) and 14-3-3σ/stratifin (SFN) was modelled with AlphaFold Multimer. The highest ranked model and its PAE score are shown. **(B)** The highest ranked AlphaFold model of the SFN-TOC site complex was used for molecular dynamics simulation. RMSD changes during the simulation run are shown. 150 frames/conformations between 85 ns and 100 ns (Δt = 100 ps) were extracted for subsequent analysis. **(C)** Combined Cα contact map of all 150 sampled conformations indicates the frequency of contacts between SFN and TOC site over time. Identified interactions between positions of TOC mutants and residues in SFN are labelled. **(D)** Visualisation of interactions between pathologically relevant residues in the wt TOC site with residues of SFN: cartoon representation of conformation at 92 ns of MD simulation. I186 interacts with a hydrophobic cleft in SFN. D188 and R197 form salt bridges. P189 shows no interaction. **(E)** Changes in overall complex stability and binding energies were calculated for the pathological TOC mutations for all 150 conformations: ΔΔG<0 indicate improved stability/binding; ΔΔG>0 indicate decreased

900 stability/binding. **(F)** Gene expression levels of 14-3-3 proteins in epidermis and primary keratinocytes
901 and primary fibroblasts. **(G)** To analyse the interaction between 14-3-3 proteins and the indicated
902 iRhom2 variants, coIPs were performed using the indicated iRhom variants (with HA tag) as bait. SFN
903 was additionally overexpressed (oe) in the indicated samples. Immunoblotting and subsequent
904 densitometric measurements were used to quantitatively analyse iRhom2-14-3-3 protein binding (ratio
905 of co-precipitated 14-3-3 protein and precipitated iRhom2) and normalised to wt iRhom2. Notably, the
906 dimeric form of oe SFN appears to be somewhat resistant to SDS.

907

908 **Figure 8: The iRhom2 N-terminal tail regulates ADAM17 binding and shedding activity.** Wt iRhom2
909 plays a critical role in regulating the transport, maturation, constitutive and simulated shedding activity
910 of ADAM17, ensuring proper control of downstream signalling pathways such as EGFR activation.
911 Conversely, disruption of the TOC site in the N-terminal tail of iRhom2 results in loss of
912 phosphorylation-independent 14-3-3 binding and appears to result in dysregulated higher constitutive
913 shedding activity. Hyperkeratosis and increased risk of OSCC, which also shows higher iRhom2 and
914 ADAM17 expression, are known consequences of TOC mutations. In the case of the cub deletion, not
915 only is the TOC site disrupted, but efficient binding to ADAM17 is also impaired, accelerating ADAM17
916 turnover and lysosomal degradation. In addition, the cub deletion loses its ability to promote
917 stimulated ADAM17 shedding activity. It is likely that the lack of phosphorylation-dependent 14-3-3
918 binding plays a key role in this process.

919

920 **Figure S1: (A)** Gene expression levels of iRhom1 (RHBDF1) and iRhom2 (RHBDF2) (see Fig. 1C) from
921 primary cell samples are shown as stacked bars, indicating that total iRhom (iRhom1 plus iRhom2)
922 expression may be regulated to a similar overall level in untreated primary cells from healthy tissue.
923 **(B)** Gene expression levels of iRhom1 (RHBDF1) and iRhom2 (RHBDF2) from untreated primary murine
924 keratinocytes from healthy tissue (n = 5), untreated primary murine fibroblasts from healthy dermis
925 tissue (n = 12) and samples from healthy murine heart tissue (n = 98) were analysed. **(C)** Gene
926 expression levels of ADAM17, AREG, TGFα, TNFα and IL6 were analysed in oesophagus and cancerous
927 oesophagus tissues (see Fig. 6C). **(D)** To test whether the increased iRhom2 expression levels were due
928 to the presence of macrophages or monocytes in the samples, the ratio between iRhom2 and CD14
929 (monocyte and macrophage markers) of the samples was calculated and compared with the values of
930 the indicated immune cell populations (Fig. S2), showing that the measured high iRhom2 levels cannot
931 be explained by the presence of immune cells.**(E)** Gene expression levels of iRhom1 (RHBDF1) and
932 iRhom2 (RHBDF2) fromHEK293 cells (n = 6).

933

934 **Figure S2:** Gene expression levels of indicated immune cell markers: CD94 (NK-cells), CD3γ (T-cells),
935 CD19 (B-cells), CD64 (monocytes/macrophages, Dendritic cells), CD14 (monocytes/macrophages,
936 granulocytes), CD66b/CD67 (granulocytes), CD170 (tumour-associated neutrophiles,
937 monocytes/macrophages, activated dendritic cells, lymphocytes-subsets) were analysed with the
938 GENEVESTIGATOR platform **(A)** in oesophagus and cancerous oesophagus tissues (see Fig. 1G) and **(B)**
939 in indicated human immune cell populations: macrophages (n = 6), granulocytes (n = 6), leukocytes
940 (n = 8) and monocytes (n = 13).

941

942 **Figure S3: (A)** Protein sequence alignment of the N-terminal region of the cytosolic tail of human
943 iRhom2 (isoform 1 and isoform 2) and murine iRhom2. **(B)** Surface localisation of iRhom2 variants (with
944 HA tag) in cells stably expressing the indicated murine constructs were measured by flow cytometry.
945 For quantification, the geometric mean of the specific fluorescence signal was determined. n > 11. **(C)**
946 Surface localisation of iRhom2 variants (with HA tag) in cells stably expressing the indicated human
947 constructs were measured by flow cytometry. For quantification, the geometric mean of the specific
948 fluorescence signal was determined. n > 5. **(D)** Immunoblot of samples from MEFs deficient for iRhom1
949 and iRhom2 stably expressing the indicated iRhom2 variants or GFP (ctr.) were used. The transferrin
950 receptor (TfR1) served as an input control. (n = 3). **(E)** To analyse the fate of mature ADAM17 in cells
951 expressing the indicated TOC mutations, cells were treated with bafilomycin ("B") for 8 h to inhibit
952 lysosomal degradation. Levels of mature ADAM17 were assessed by densitometric measurements and
953 calculation of the ratio between mature ADAM17 and the loading control GAPDH, which is independent
954 of lysosomal degradation. (n > 4). **(F)** To assess the turn-over rate of ADAM17 a cycloheximide-based
955 (Chx) pulse-chase experiment was performed. Reduction of ADAM17 levels was assessed by
956 densitometric measurements and normalisation to 0 h Chx treatment (set to 1). (n = 5).

957 **Figure S4: (A)** ADAM17 levels of immunoblot (Fig. 6C) were assessed by densitometric measurements
958 and calculation of the ratio between total ADAM17 (mature plus immature ADAM17) divided by the
959 respective input control. Values were normalised to the respective wt-iRhom2 sample. n > 5. **(B-C)** To
960 analyse interaction between ADAM17 and the indicated iRhom2 variants, coIPs were performed using
961 the iRhom variants (with HA tag) as bait. Immunoblotting and subsequent densitometric
962 measurements were used to quantitatively analyse iRhom2-ADAM17 binding (ratio of co-precipitated
963 ADAM17 and precipitated iRhom2) and normalised to wt-iRhom2. **(B)** MEFs from mice deficient for
964 iRhom1 and iRhom2 stably expressing indicated iRhom2 variants with ER retention signal KDEL or GFP
965 (ctr.) were used (n = 4). **(C)** iRhom-ADAM17 binding after lysosomal inhibition was analysed.
966 Densitometric measurements of coIP immunoblot (Fig. 6D) (n = 4).

967

References

Abd Alla, J., et al. (2016). J Biol Chem **291**(6): 2583-2600 DOI: 10.1074/jbc.M115.702688.
Adrain, C., et al. (2012). Science **335**(6065): 225-228 DOI: 10.1126/science.1214400.
Alcendor, R. R., et al. (2007). Circ Res **100**(10): 1512-1521 DOI: 10.1161/01.RES.0000267723.65696.4a.
Allende, M. L., et al. (2013). J Biol Chem **288**(25): 18381-18391 DOI: 10.1074/jbc.M113.478420.
Arakawa, K., et al. (2023). Genes Cells DOI: 10.1111/gtc.13050.
Arcidiacono, P., et al. (2018). Nat Commun **9**(1): 1021 DOI: 10.1038/s41467-018-03470-y.
Arndt, P. G., et al. (2011). PLoS One **6**(5): e19938 DOI: 10.1371/journal.pone.0019938.
Babendreyer, A., et al. (2020). Front Cardiovasc Med **7**: 610344 DOI: 10.3389/fcvm.2020.610344.
Barger, J. L., et al. (2008). PLoS One **3**(6): e2264 DOI: 10.1371/journal.pone.0002264.
Black, R. A., et al. (1997). Nature **385**(6618): 729-733 DOI: 10.1038/385729a0.
Blaydon, D. C., et al. (2011). N Engl J Med **365**(16): 1502-1508 DOI: 10.1056/NEJMoa1100721.
Blaydon, D. C., et al. (2012). Am J Hum Genet **90**(2): 340-346 DOI: 10.1016/j.ajhg.2011.12.008.
Bosse, Y., et al. (2007). Physiol Genomics **29**(2): 161-168 DOI: 10.1152/physiolgenomics.00134.2006.
Brooke, M. A., et al. (2014). Hum Mol Genet **23**(15): 4064-4076 DOI: 10.1093/hmg/ddu120.
Busch, H., et al. (2008). Mol Syst Biol **4**: 199 DOI: 10.1038/msb.2008.36.
Cavadas, M., et al. (2017). Cell Rep **21**(3): 745-757 DOI: 10.1016/j.celrep.2017.09.074.
Chao-Chu, J., et al. (2021). J Invest Dermatol **141**(4): 722-726 DOI: 10.1016/j.jid.2020.09.010.
Chen, Y., et al. (2008). BMC Genomics **9**: 264 DOI: 10.1186/1471-2164-9-264.
Christova, Y., et al. (2013). EMBO Rep **14**(10): 884-890 DOI: 10.1038/embor.2013.128.
Cock, P. J., et al. (2009). Bioinformatics **25**(11): 1422-1423 DOI: 10.1093/bioinformatics/btp163.
Dosztanyi, Z., et al. (2009). Bioinformatics **25**(20): 2745-2746 DOI: 10.1093/bioinformatics/btp518.
Dufour, C. R., et al. (2007). Cell Metab **5**(5): 345-356 DOI: 10.1016/j.cmet.2007.03.007.
Dulloo, I., et al. (2022). bioRxiv: 2022.2011.2028.518246 DOI: 10.1101/2022.11.28.518246.
Düsterhöft, S., et al. (2021). Cell Mol Life Sci DOI: 10.1007/s00018-021-03845-3.
Düsterhöft, S., et al. (2019). Pathol Res Pract **215**(6): 152410 DOI: 10.1016/j.prp.2019.04.002.
Dyson, H. J. (2016). Biophys J **110**(5): 1013-1016 DOI: 10.1016/j.bpj.2016.01.030.
Ellis, A., et al. (1994). Eur J Cancer B Oral Oncol **30B**(2): 102-112 DOI: 10.1016/0964-1955(94)90061-2.
Ellis, A., et al. (2015). Orphanet J Rare Dis **10**: 126 DOI: 10.1186/s13023-015-0346-2.
Erdos, G., et al. (2021). Nucleic Acids Res **49**(W1): W297-W303 DOI: 10.1093/nar/gkab408.
Esaki, H., et al. (2015). J Allergy Clin Immunol **135**(1): 153-163 DOI: 10.1016/j.jaci.2014.10.037.
Gambino, V., et al. (2013). Aging Cell **12**(3): 435-445 DOI: 10.1111/acel.12060.
Garinis, G. A., et al. (2009). Nat Cell Biol **11**(5): 604-615 DOI: 10.1038/ncb1866.
Giese, A. A., et al. (2021). Sci Rep **11**(1): 24230 DOI: 10.1038/s41598-021-03522-2.
Grieve, A., et al. (2017). Elife **6** DOI: 10.7554/eLife.23968.
Guo, A., et al. (2014). Mol Cell Proteomics **13**(1): 372-387 DOI: 10.1074/mcp.O113.027870.
Henrichsen, C. N., et al. (2011). PLoS Comput Biol **7**(1): e1001054 DOI: 10.1371/journal.pcbi.1001054.
Ho, S. N., et al. (1989). Gene **77**(1): 51-59 DOI: 10.1016/0378-1119(89)90358-2.
Hornbeck, P. V., et al. (2015). Nucleic Acids Res **43**(Database issue): D512-520 DOI: 10.1093/nar/gku1267.
Hosur, V., et al. (2018a). FEBS Open Bio **8**(4): 702-710 DOI: 10.1002/2211-5463.12407.
Hosur, V., et al. (2018b). Front Genet **9**: 233 DOI: 10.3389/fgene.2018.00233.
Hosur, V., et al. (2014). Proc Natl Acad Sci U S A **111**(21): E2200-2209 DOI: 10.1073/pnas.1323908111.
Hosur, V., et al. (2017). Biol Open **6**(8): 1174-1179 DOI: 10.1242/bio.026260.
Howel-Evans, W., et al. (1958). Q J Med **27**(107): 413-429.
Hruz, T., et al. (2008). Adv Bioinformatics **2008**: 420747 DOI: 10.1155/2008/420747.
Inada, M., et al. (2016). Int J Mol Med **37**(6): 1521-1527 DOI: 10.3892/ijmm.2016.2568.
Issuree, P. D., et al. (2013). J Clin Invest **123**(2): 928-932 DOI: 10.1172/JCI66168.
Jocher, G., et al. (2022). EMBO Rep **23**(6): e54305 DOI: 10.15252/embr.202154305.

Johnson, K. R., et al. (2003). Genomics **81**(1): 6-14 DOI: 10.1016/S0888-7543(02)00013-7.
Jumper, J., et al. (2021). Nature **596**(7873): 583-589 DOI: 10.1038/s41586-021-03819-2.
Kahveci-Türköz, S., et al. (2023). Cell Mol Life Sci **80**(5): 135 DOI: 10.1007/s00018-023-04783-y.
Ketteler, R., et al. (2002). Gene Ther **9**(8): 477-487 DOI: 10.1038/sj.gt.3301653.
Klausen, M. S., et al. (2019). Proteins **87**(6): 520-527 DOI: 10.1002/prot.25674.
Ku, N. O., et al. (2002). Proc Natl Acad Sci U S A **99**(7): 4373-4378 DOI: 10.1073/pnas.072624299.
Kubo, S., et al. (2022). Nat Immunol **23**(1): 75-85 DOI: 10.1038/s41590-021-01093-y.
Künzel, U., et al. (2018). Elife **7** DOI: 10.7554/eLife.35012.
Lambert, D. W., et al. (2005). J Biol Chem **280**(34): 30113-30119 DOI: 10.1074/jbc.M505111200.
Lattin, J. E., et al. (2008). Immunome Res **4**: 5 DOI: 10.1186/1745-7580-4-5.
Li, X., et al. (2017). J Cell Sci **130**(5): 868-878 DOI: 10.1242/jcs.196436.
Li, X., et al. (2015). Proc Natl Acad Sci U S A **112**(19): 6080-6085 DOI: 10.1073/pnas.1505649112.
Lindorff-Larsen, K., et al. (2010). Proteins **78**(8): 1950-1958 DOI: 10.1002/prot.22711.
Lu, X. L., et al. (2017). Biomed Pharmacother **86**: 645-653 DOI: 10.1016/j.biopha.2016.11.075.
Lucas, E., et al. (2014). Biochim Biophys Acta **1842**(12 Pt A): 2448-2456 DOI: 10.1016/j.bbadis.2014.09.004.
Maney, S. K., et al. (2015). Sci Signal **8**(401): ra109 DOI: 10.1126/scisignal.aac5356.
Marchina, E., et al. (2014). J Neurol Sci **337**(1-2): 42-46 DOI: 10.1016/j.jns.2013.11.014.
Maretzky, T., et al. (2013). Proc Natl Acad Sci U S A **110**(28): 11433-11438 DOI: 10.1073/pnas.1302553110.
Maruthappu, T., et al. (2017). Nat Commun **8**: 14174 DOI: 10.1038/ncomms14174.
McIlwain, D. R., et al. (2012). Science **335**(6065): 229-232 DOI: 10.1126/science.1214448.
Mercader, J. M., et al. (2012). PLoS Genet **8**(12): e1003046 DOI: 10.1371/journal.pgen.1003046.
Meszaros, B., et al. (2018). Nucleic Acids Res **46**(W1): W329-W337 DOI: 10.1093/nar/gky384.
Meszaros, B., et al. (2009). PLoS Comput Biol **5**(5): e1000376 DOI: 10.1371/journal.pcbi.1000376.
Mirdita, M., et al. (2022). Nat Methods **19**(6): 679-682 DOI: 10.1038/s41592-022-01488-1.
Mokoena, T., et al. (2018). Clin Genet **93**(5): 1114-1116 DOI: 10.1111/cge.13161.
Muchir, A., et al. (2007). Hum Mol Genet **16**(15): 1884-1895 DOI: 10.1093/hmg/ddm137.
Nguyen Ba, A. N., et al. (2009). BMC Bioinformatics **10**: 202 DOI: 10.1186/1471-2105-10-202.
Niehues, R. V., et al. (2022). FASEB J **36**(3): e22234 DOI: 10.1096/fj.202101521R.
Obsilova, V. and T. Obsil (2022). Front Mol Biosci **9**: 1016071 DOI: 10.3389/fmolb.2022.1016071.
Oikonomidi, I., et al. (2018). Elife **7** DOI: 10.7554/eLife.35032.
Oka, S., et al. (2011). Cell Metab **14**(5): 598-611 DOI: 10.1016/j.cmet.2011.10.001.
Palau, V., et al. (2020). Nephrol Dial Transplant **35**(6): 1071-1072 DOI: 10.1093/ndt/gfaa093.
Peschon, J. J., et al. (1998). Science **282**(5392): 1281-1284 DOI: 10.1126/science.282.5392.1281.
Pettersen, E. F., et al. (2021). Protein Sci **30**(1): 70-82 DOI: 10.1002/pro.3943.
Pronk, S., et al. (2013). Bioinformatics **29**(7): 845-854 DOI: 10.1093/bioinformatics/btt055.
Qu, L., et al. (2019). Acta Derm Venereol **99**(7): 699-700 DOI: 10.2340/00015555-3189.
Rabinowitsch, A. I., et al. (2023). J Cell Sci DOI: 10.1242/jcs.260910.
Ramchandran, R., et al. (2006). Proc Natl Acad Sci U S A **103**(50): 19087-19092 DOI: 10.1073/pnas.0602715103.
Ricard, G., et al. (2010). PLoS Biol **8**(11): e1000543 DOI: 10.1371/journal.pbio.1000543.
Rizza, S., et al. (2015). Atherosclerosis **239**(2): 459-464 DOI: 10.1016/j.atherosclerosis.2015.01.029.
Roth, R. B., et al. (2006). Neurogenetics **7**(2): 67-80 DOI: 10.1007/s10048-006-0032-6.
Ruijter, J. M., et al. (2009). Nucleic Acids Res **37**(6): e45 DOI: 10.1093/nar/gkp045.
Sa, S. M., et al. (2007). J Immunol **178**(4): 2229-2240 DOI: 10.4049/jimmunol.178.4.2229.
Saarinen, S., et al. (2012). Fam Cancer **11**(3): 525-528 DOI: 10.1007/s10689-012-9532-8.
Sahin, U., et al. (2004). J Cell Biol **164**(5): 769-779 DOI: 10.1083/jcb.200307137.
Sato, T., et al. (2013). Sci Rep **3**: 1911 DOI: 10.1038/srep01911.
Schmitt, L., et al. (2018). Lasers Med Sci **33**(4): 765-772 DOI: 10.1007/s10103-017-2409-1.
Schumacher, N., et al. (2023). Biochim Biophys Acta Mol Cell Res: 119489 DOI: 10.1016/j.bbamcr.2023.119489.

Shalhoub, V., et al. (2010). J Cell Biochem **111**(4): 911-921 DOI: 10.1002/jcb.22779.
Shuai, Y., et al. (2011). Toxicol Lett **200**(1-2): 77-87 DOI: 10.1016/j.toxlet.2010.10.017.
Sieber, B., et al. (2022). J Cell Sci **135**(17) DOI: 10.1242/jcs.259949.
Sievers, F., et al. (2011). Mol Syst Biol **7**: 539 DOI: 10.1038/msb.2011.75.
Siggs, O. M., et al. (2014). Biol Open **3**(12): 1151-1157 DOI: 10.1242/bio.201410116.
Siggs, O. M., et al. (2012). Blood **119**(24): 5769-5771 DOI: 10.1182/blood-2012-03-417949.
Smith, J. C., et al. (2008). J Invest Dermatol **128**(5): 1298-1310 DOI: 10.1038/sj.jid.5701149.
Smyth, E. C., et al. (2017). Nat Rev Dis Primers **3**: 17048 DOI: 10.1038/nrdp.2017.48.
Strunnikova, N. V., et al. (2009). PLoS One **4**(12): e8402 DOI: 10.1371/journal.pone.0008402.
Swindell, W. R., et al. (2012). PLoS One **7**(3): e34594 DOI: 10.1371/journal.pone.0034594.
Tang, B., et al. (2020). FASEB J **34**(4): 4956-4969 DOI: 10.1096/fj.201902649R.
Thorrez, L., et al. (2008). PLoS One **3**(3): e1854 DOI: 10.1371/journal.pone.0001854.
Traister, A., et al. (2013). PLoS One **8**(11): e77331 DOI: 10.1371/journal.pone.0077331.
Uhlenhopp, D. J., et al. (2020). Clin J Gastroenterol **13**(6): 1010-1021 DOI: 10.1007/s12328-020-01237-x.
Vallender, T. W. and B. T. Lahn (2006). FEBS Lett **580**(18): 4560-4566 DOI: 10.1016/j.febslet.2006.07.017.
Van Durme, J., et al. (2011). Bioinformatics **27**(12): 1711-1712 DOI: 10.1093/bioinformatics/btr254.
Verkerk, A. J., et al. (2009). Am J Hum Genet **85**(1): 40-52 DOI: 10.1016/j.ajhg.2009.06.004.
Visser, R., et al. (2012). PLoS One **7**(11): e49229 DOI: 10.1371/journal.pone.0049229.
Voets, A. M., et al. (2012). Biochim Biophys Acta **1822**(7): 1161-1168 DOI: 10.1016/j.bbadis.2011.10.009.
Wang, L., et al. (2016). Sci Rep **6**: 28399 DOI: 10.1038/srep28399.
Wang, Q., et al. (2013). BMC Cancer **13**: 137 DOI: 10.1186/1471-2407-13-137.
Wang, X. M., et al. (2012). Stem Cell Res Ther **3**(5): 39 DOI: 10.1186/scrt130.
Wong, J., et al. (2010). Crit Care Med **38**(1): 25-31 DOI: 10.1097/CCM.0b013e3181b427e8.
Yang, T., et al. (2022). J Transl Med **20**(1): 127 DOI: 10.1186/s12967-022-03311-z.
Yuan, F., et al. (2021). PLoS Pathog **17**(3): e1009393 DOI: 10.1371/journal.ppat.1009393.
Yunoki, T., et al. (2018). Oncol Lett **16**(5): 6729-6734 DOI: 10.3892/ol.2018.9484.
Zanotti, A., et al. (2022). Science **378**(6623): 996-1000 DOI: 10.1126/science.abo5672.
Zaruba, M., et al. (2022). Viruses **14**(2) DOI: 10.3390/v14020381.
Zhao, Y., et al. (2007). Cell **129**(2): 303-317 DOI: 10.1016/j.cell.2007.03.030.

Figure 1

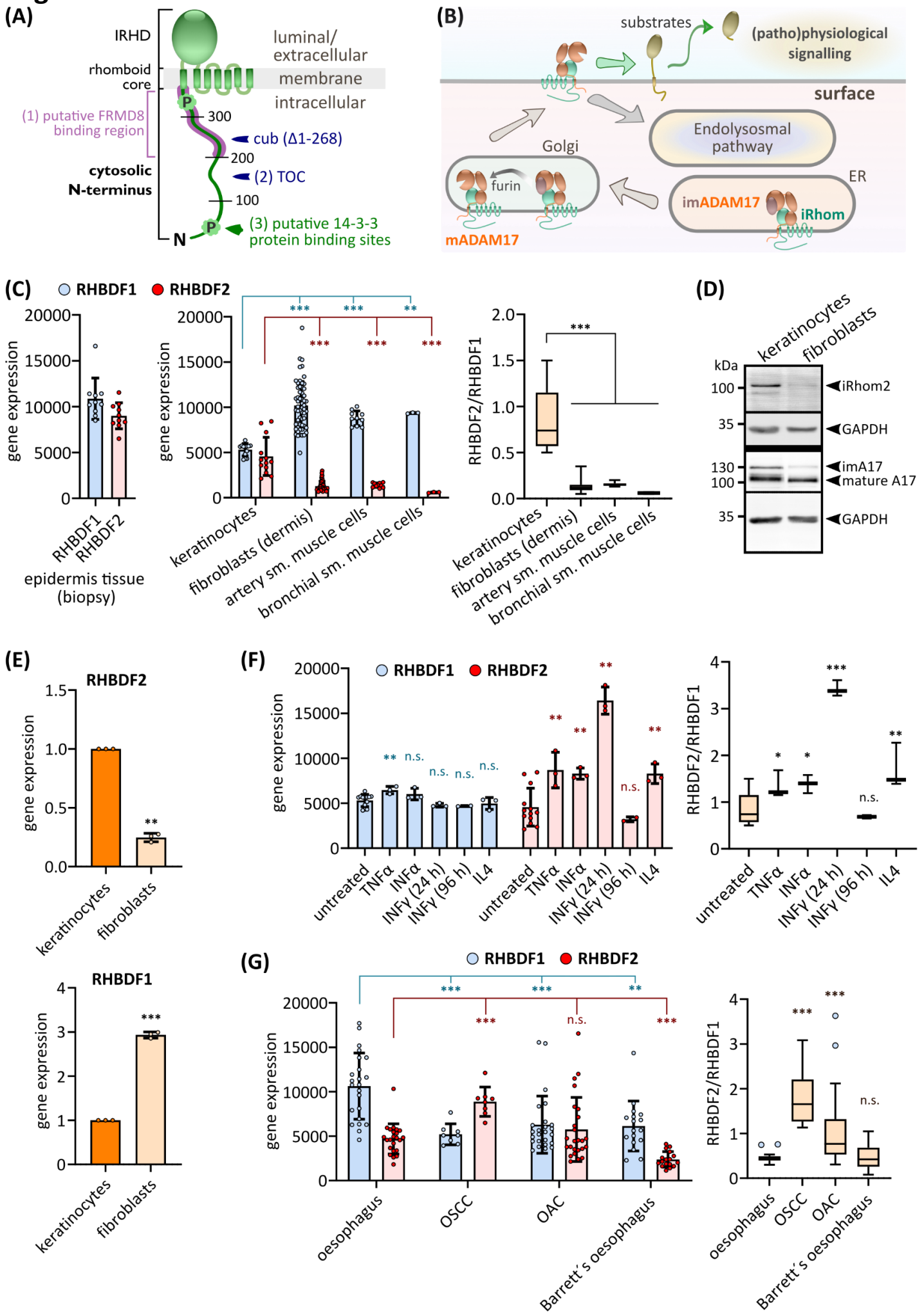
(A)
IRHD
luminal/ extracellular
rhomboid core
membrane
intracellular
(1) putative FRMD8 binding region
300
cub (Δ1-268)
200
(2) TOC
cytosolic N-terminus
100
(3) putative 14-3-3 protein binding sites
N
(B)
substrates
(patho)physiological signalling
surface
Endolysosmal pathway
Golgi
furin
ER
imADAM17
iRhom
mADAM17
(C)
RHBDF1
RHBDF2
gene expression
RHBDF1
RHBDF2
epidermis tissue (biopsy)
keratinocytes
fibroblasts (dermis)
artery sm. muscle cells
bronchial sm. muscle cells
RHBDF2/RHBDF1
(D)
keratinocytes
fibroblasts
kDa
iRhom2
GAPDH
imA17
mature A17
GAPDH
(E)
RHBDF2
RHBDF1
keratinocytes
fibroblasts
(F)
untreated
TNFα
INFα
INFγ (24 h)
INFγ (96 h)
IL4
n.s.
(G)
oesophagus
OSCC
OAC
Barrett´s oesophagus

Figure 2

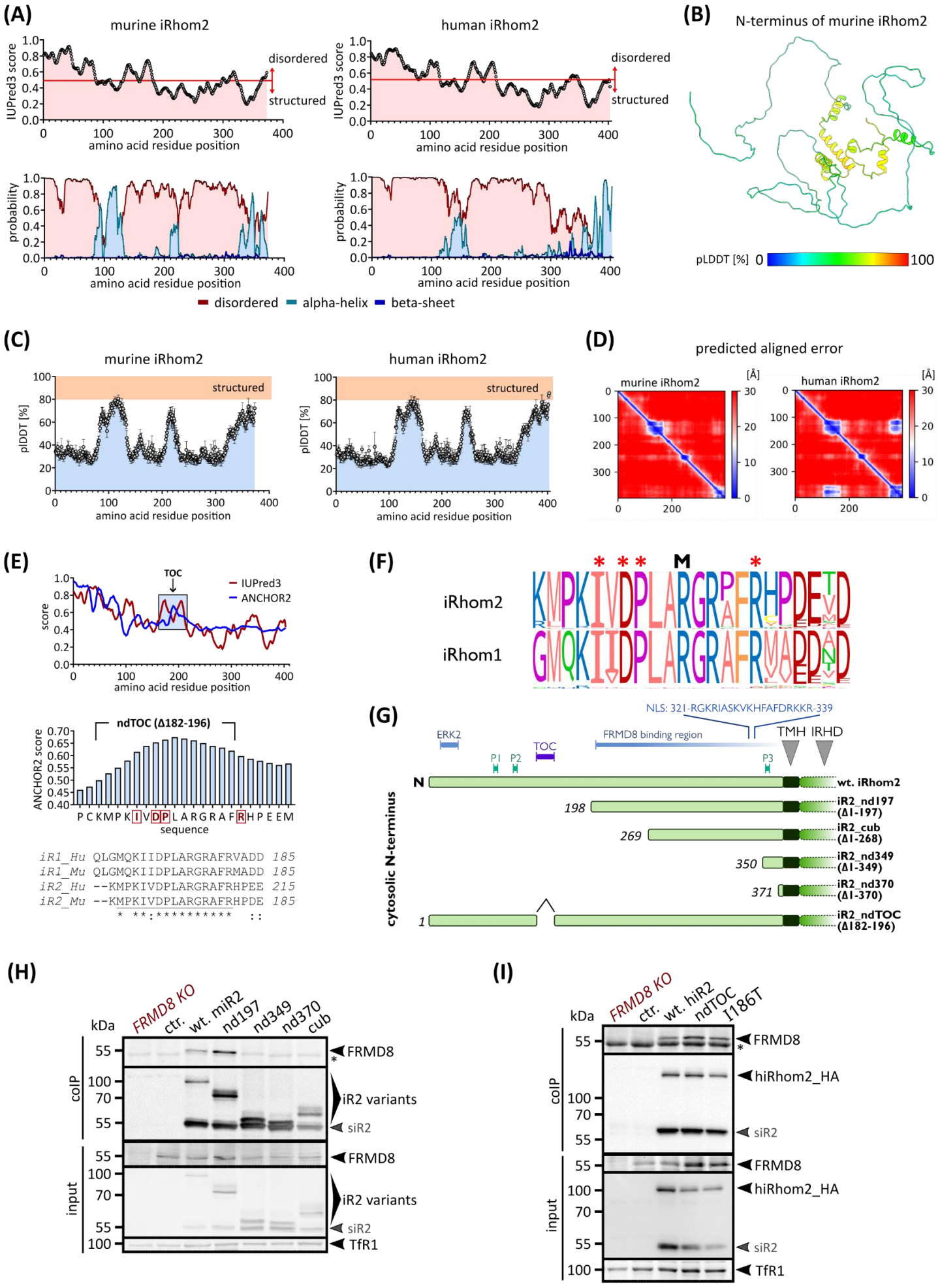
(A)
murine iRhom2
human iRhom2
IUPred3 score
disordered
structured
amino acid residue position
probability
disordered
alpha-helix
beta-sheet
(B)
N-terminus of murine iRhom2
pLDDT [%]
0
100
(C)
murine iRhom2
human iRhom2
pIDDT [%]
structured
amino acid residue position
(D)
predicted aligned error
murine iRhom2
human iRhom2
[Å]
(E)
TOC
IUPred3
ANCHOR2
score
amino acid residue position
ndTOC (Δ182-196)
ANCHOR2 score
P C K M P K I V D P L A R G R A F R H P E E M
sequence
iR1_Hu QLGMQKIIDPLARGRAFRVADD 185
iR1_Mu QLGMQKIIDPLARGRAFRMADD 185
iR2_Hu --KMPKIVDPLARGRAFRHPEE 215
iR2_Mu --KMPKIVDPLARGRAFRHPDE 185
(F)
iRhom2
iRhom1
(G)
NLS: 321-RGKRIASKVKHFAFDRKKR-339
ERK2
FRMD8 binding region
TMH
IRHD
TOC
P1
P2
P3
N
cytosolic N-terminus
wt. iRhom2
198
iR2_nd197 (Δ1-197)
269
iR2_cub (Δ1-268)
350
iR2_nd349 (Δ1-349)
371
iR2_nd370 (Δ1-370)
1
iR2_ndTOC (Δ182-196)
(H)
kDa
FRMD8 KO
ctr.
wt. miR2
nd197
nd349
nd370
cub
coIP
input
FRMD8
iR2 variants
siR2
TfR1
(I)
kDa
FRMD8 KO
ctr.
wt. hiR2
ndTOC
I186T
coIP
input
FRMD8
hiRhom2_HA
siR2
TfR1

Figure 3

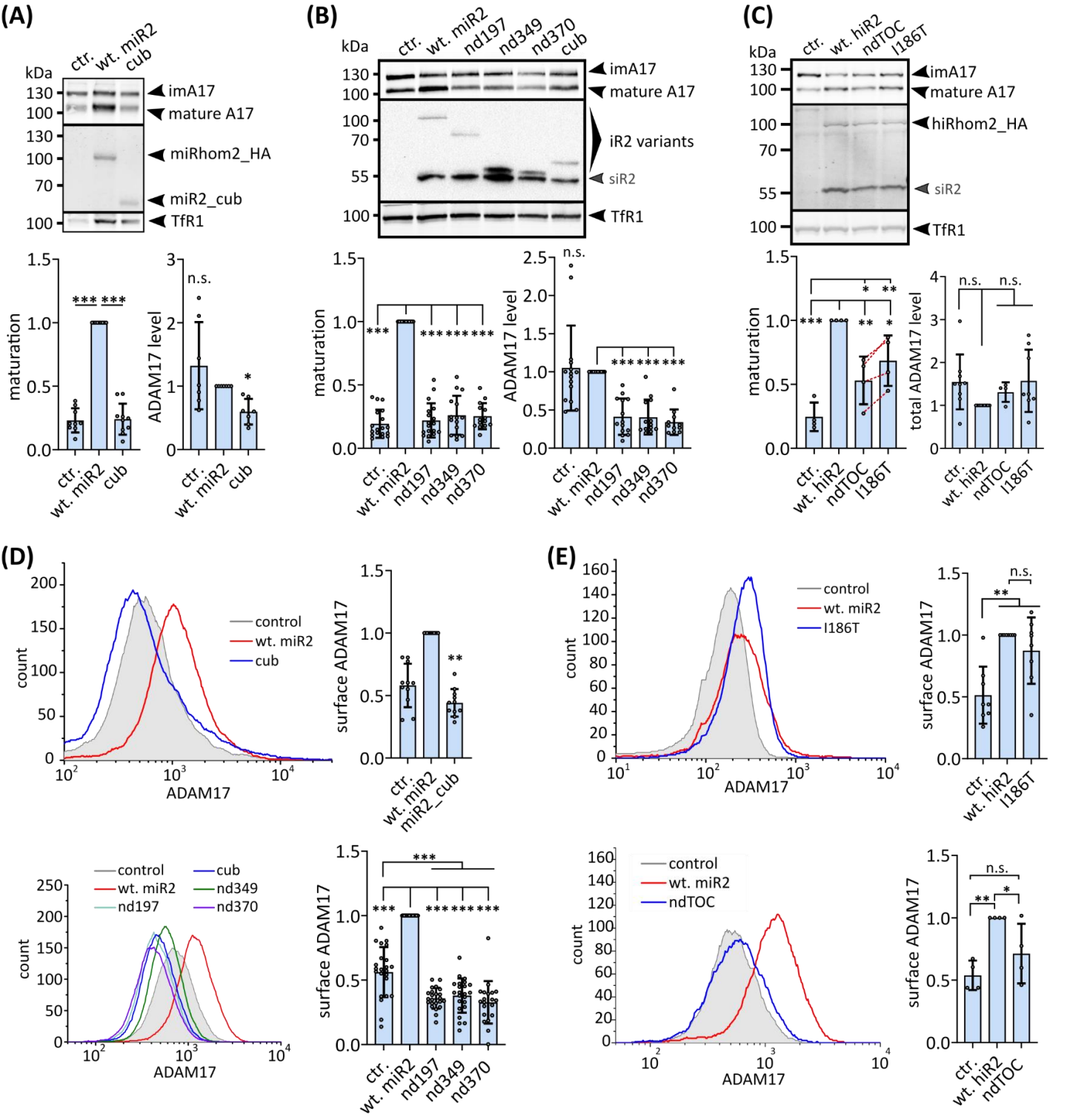
(A)
ctr.
wt. miR2
cub
kDa
130
100
imA17
mature A17
miRhom2_HA
miR2_cub
TfR1
maturation
ADAM17 level
n.s.
(B)
nd197
nd349
nd370
iR2 variants
siR2
(C)
wt. hiR2
ndTOC
I186T
hiRhom2_HA
total ADAM17 level
(D)
control
count
ADAM17
surface ADAM17
miR2_cub
(E)

Figure 4

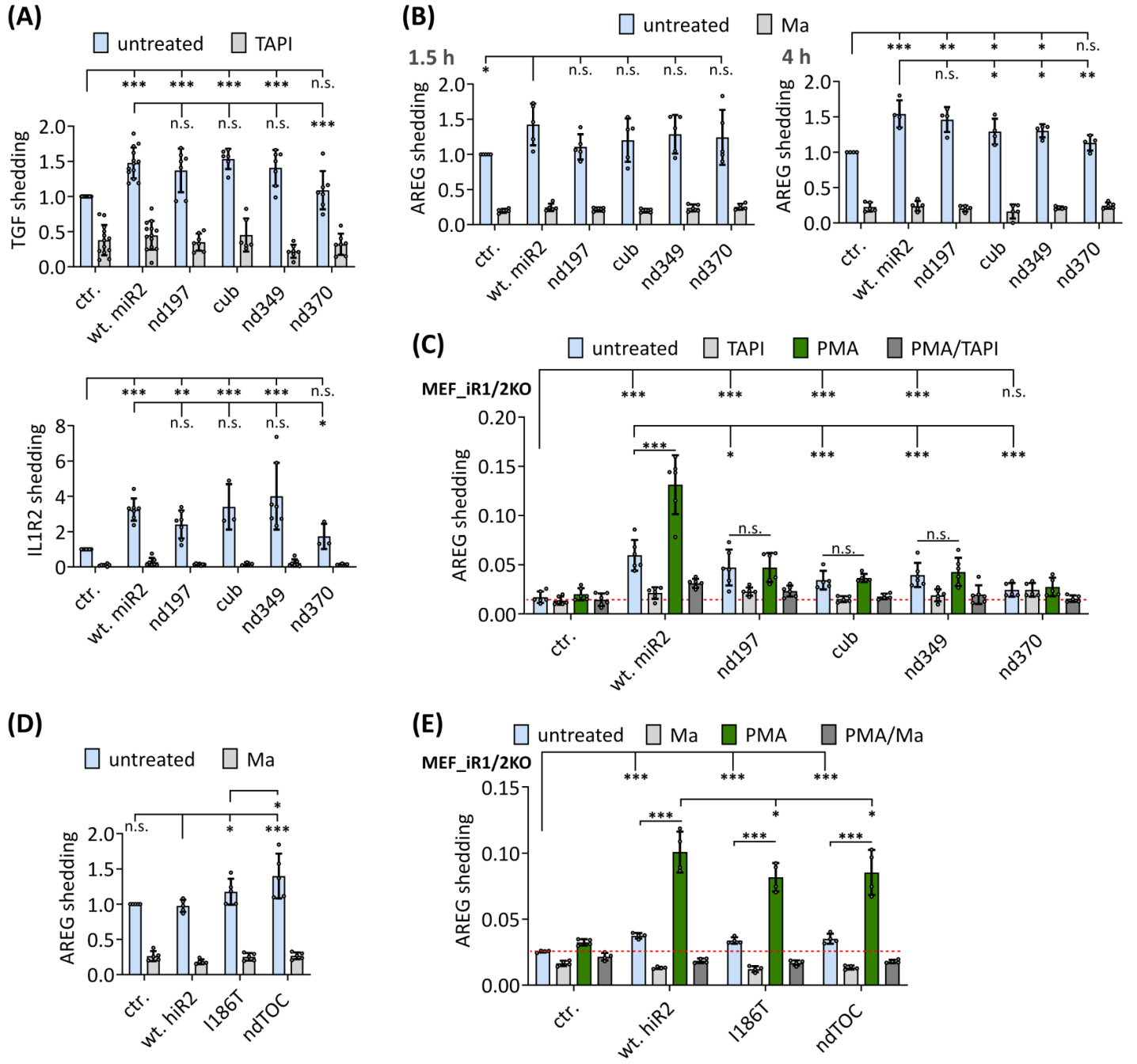
(A)
untreated
TAPI
TGF shedding
IL1R2 shedding
ctr.
wt. miR2
nd197
cub
nd349
nd370
(B)
untreated
Ma
1.5 h
4 h
AREG shedding
(C)
untreated
TAPI
PMA
PMA/TAPI
MEF_iR1/2KO
AREG shedding
(D)
untreated
Ma
AREG shedding
ctr.
wt. hiR2
I186T
ndTOC
(E)
untreated
Ma
PMA
PMA/Ma
MEF_iR1/2KO
AREG shedding

Figure 5

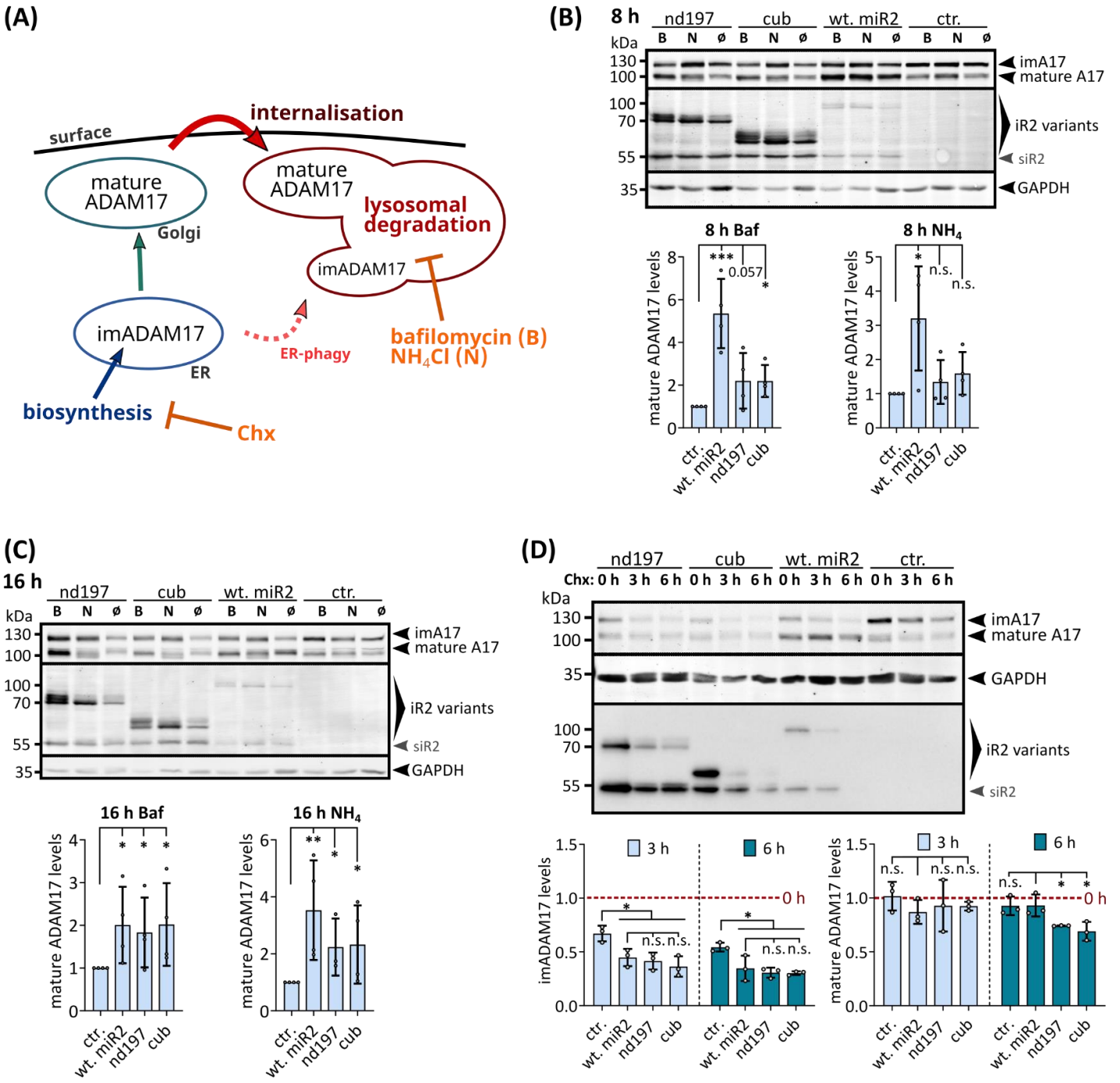
(A)
surface
internalisation
mature ADAM17
Golgi
mature ADAM17
lysosomal degradation
imADAM17
imADAM17
ER
ER-phagy
bafilomycin (B)
NH4Cl (N)
biosynthesis
Chx
(B)
8 h
nd197
cub
wt. miR2
ctr.
B N ø B N ø B N ø B N ø
kDa
130
100
100
70
55
35
imA17
mature A17
iR2 variants
siR2
GAPDH
8 h Baf
8 h NH4
mature ADAM17 levels
***
0.057
*
n.s.
ctr.
wt. miR2
nd197
cub
(C)
16 h
nd197
cub
wt. miR2
ctr.
B N ø B N ø B N ø B N ø
kDa
130
100
100
70
55
35
imA17
mature A17
iR2 variants
siR2
GAPDH
16 h Baf
16 h NH4
mature ADAM17 levels
**
*
ctr.
wt. miR2
nd197
cub
(D)
nd197
cub
wt. miR2
ctr.
Chx: 0 h 3 h 6 h 0 h 3 h 6 h 0 h 3 h 6 h 0 h 3 h 6 h
kDa
130
100
35
100
70
55
imA17
mature A17
GAPDH
iR2 variants
siR2
3 h
6 h
imADAM17 levels
mature ADAM17 levels
0 h
n.s.
*
ctr.
wt. miR2
nd197
cub

Figure 6

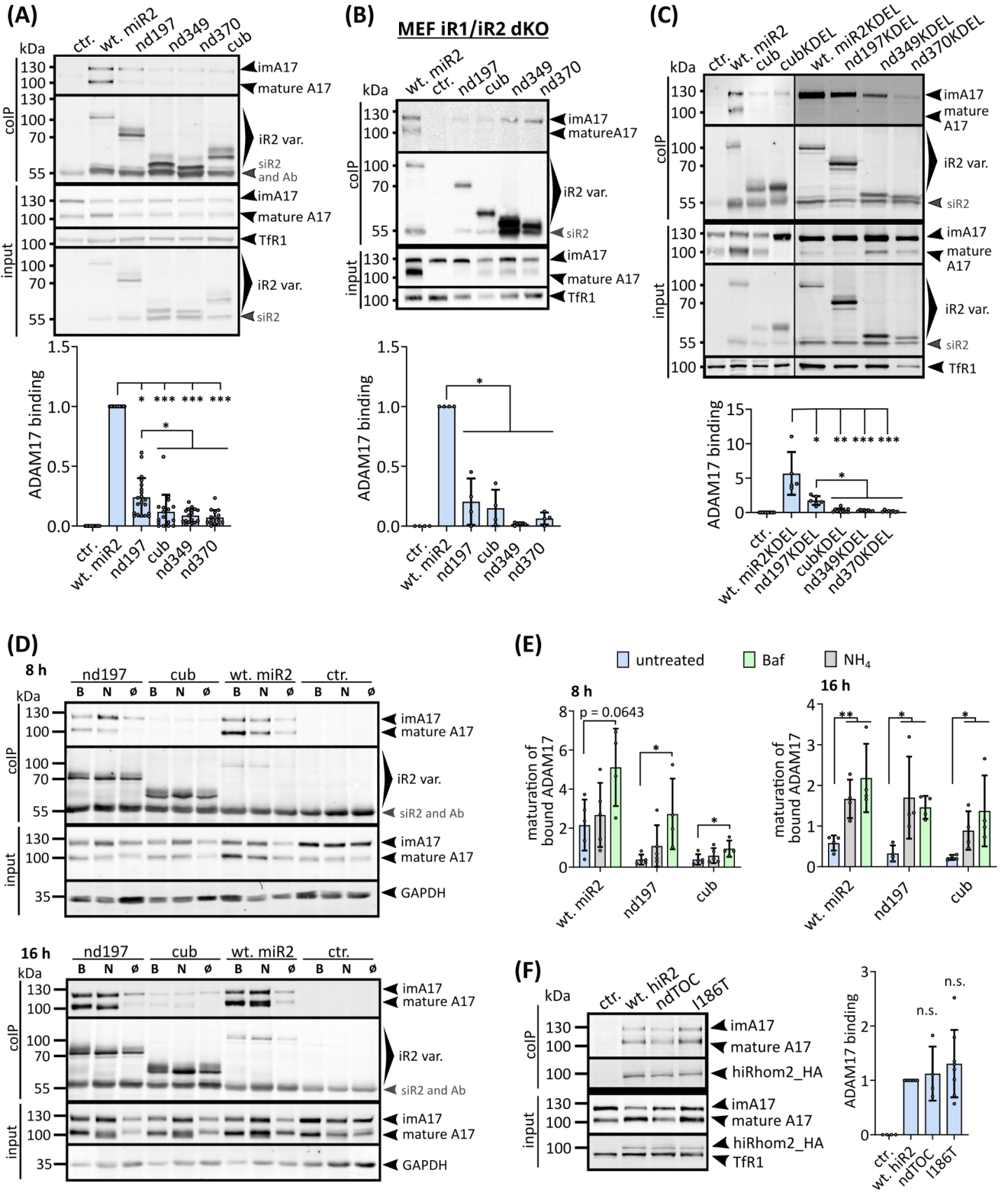
(A)
ctr.
wt. miR2
nd197
nd349
nd370
cub
kDa
130
100
70
55
colP
input
imA17
mature A17
iR2 var.
siR2 and Ab
TfR1
siR2
ADAM17 binding
(B)
MEF iR1/iR2 dKO
wt. miR2
ctr.
nd197
cub
nd349
nd370
matureA17
(C)
cubKDEL
wt. miR2KDEL
nd197KDEL
nd349KDEL
nd370KDEL
wt. miR2KDEL
nd197KDEL
cubKDEL
nd349KDEL
nd370KDEL
(D)
8 h
16 h
B
N
ø
GAPDH
35
(E)
untreated
Baf
NH4
p = 0.0643
maturation of bound ADAM17
(F)
wt. hiR2
ndTOC
I186T
hiRhom2_HA
n.s.

Figure 7

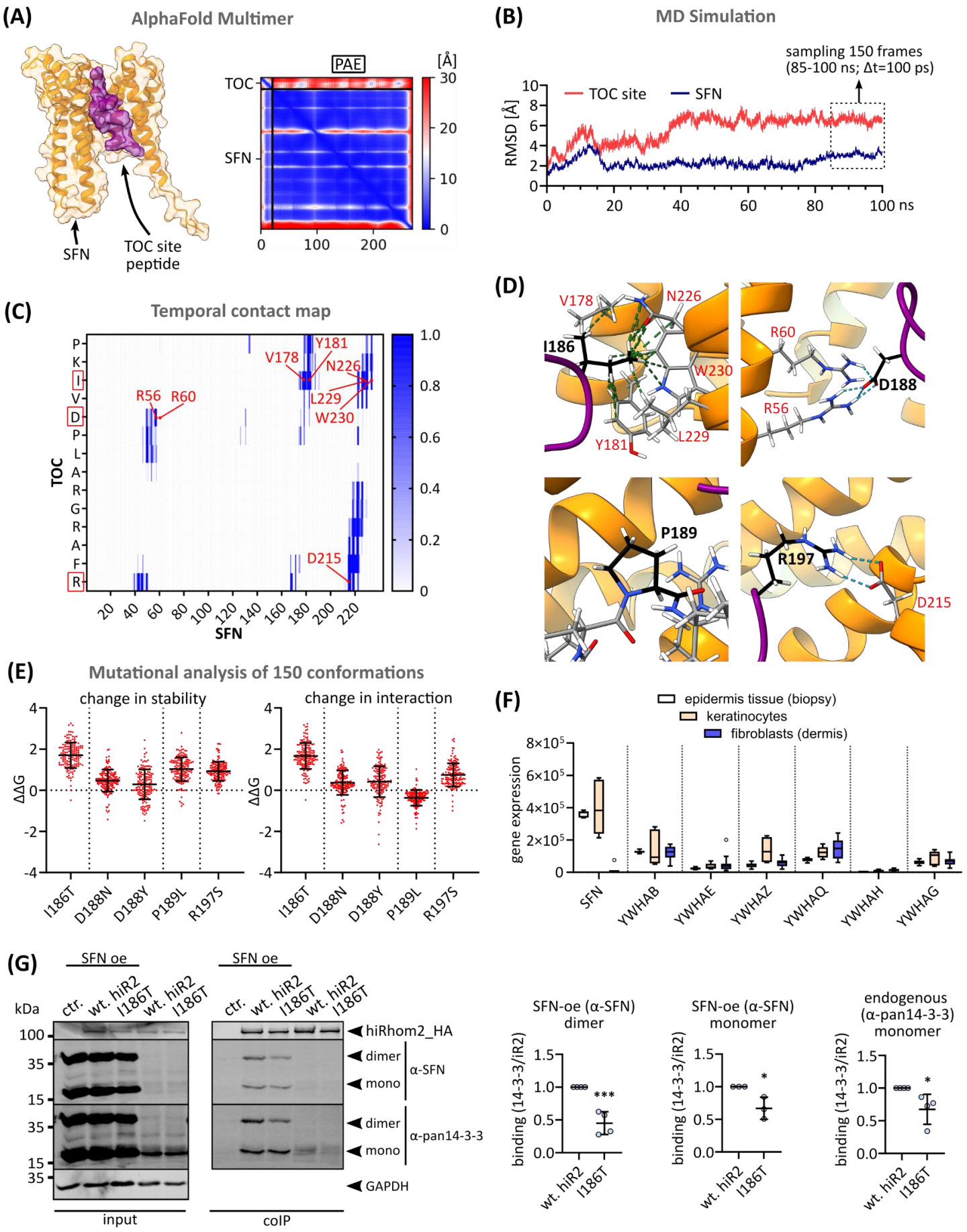
(A)
AlphaFold Multimer
SFN
TOC site peptide
PAE
[Å]
TOC
SFN
(B)
MD Simulation
sampling 150 frames (85-100 ns; Δt=100 ps)
TOC site
SFN
RMSD [Å]
100 ns
(C)
Temporal contact map
TOC
SFN
V178
Y181
N226
R56
R60
L229
W230
D215
(D)
V178
N226
I186
W230
Y181
L229
R60
D188
R56
P189
R197
D215
(E)
Mutational analysis of 150 conformations
change in stability
change in interaction
ΔΔG
I186T
D188N
D188Y
P189L
R197S
(F)
epidermis tissue (biopsy)
keratinocytes
fibroblasts (dermis)
gene expression
SFN
YWHAB
YWHAE
YWHAZ
YWHAQ
YWHAH
YWHAG
(G)
SFN oe
kDa
ctr.
wt. hiR2
I186T
hiRhom2_HA
dimer
mono
α-SFN
α-pan14-3-3
GAPDH
input
coIP
SFN-oe (α-SFN) dimer
SFN-oe (α-SFN) monomer
endogenous (α-pan14-3-3) monomer
binding (14-3-3/iR2)

Figure 8

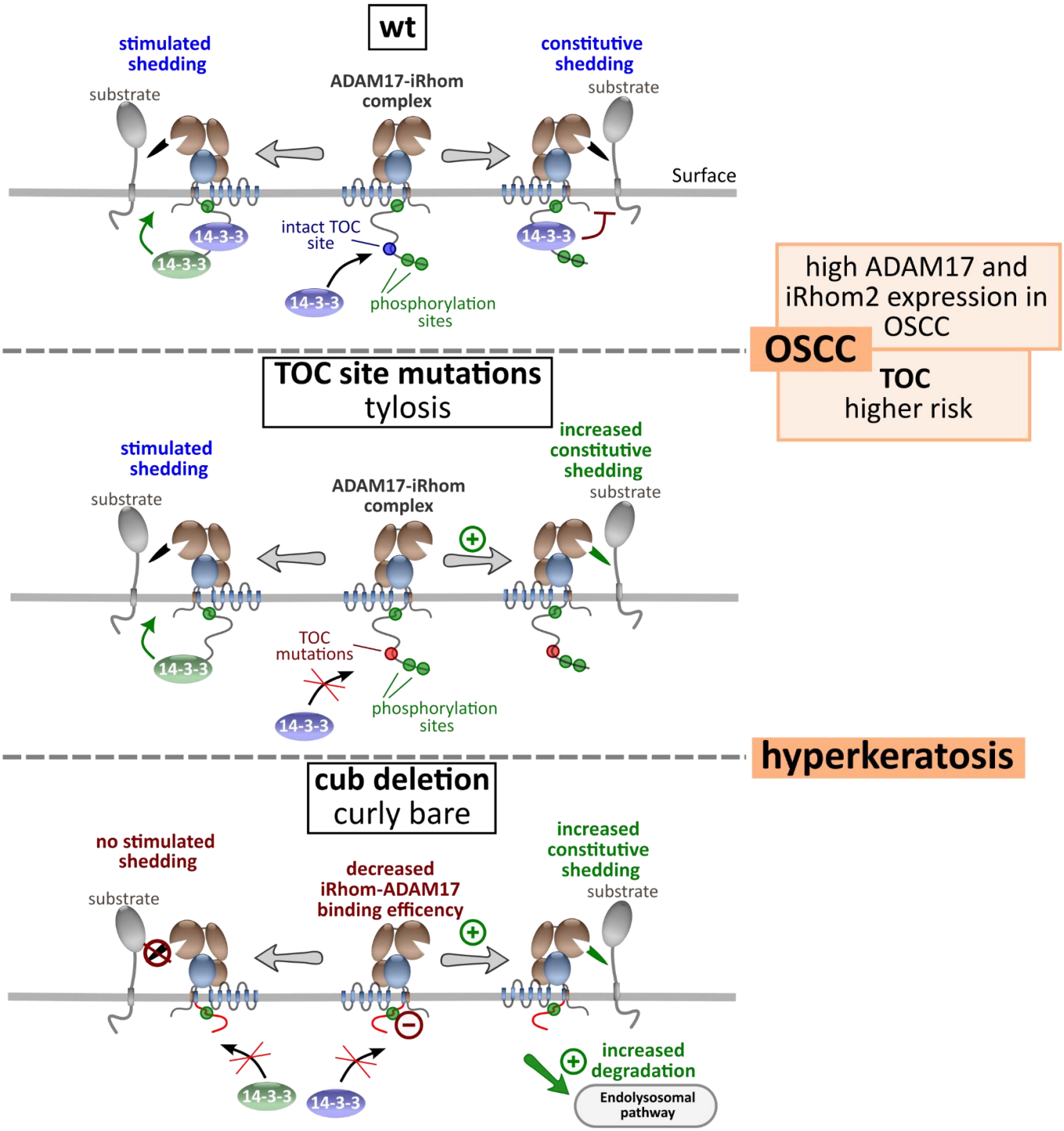
wt
stimulated shedding
substrate
ADAM17-iRhom complex
constitutive shedding
substrate
Surface
14-3-3
14-3-3
intact TOC site
14-3-3
phosphorylation sites
14-3-3
high ADAM17 and iRhom2 expression in OSCC
OSCC
TOC higher risk
TOC site mutations
tylosis
stimulated shedding
substrate
ADAM17-iRhom complex
increased constitutive shedding
substrate
14-3-3
TOC mutations
14-3-3
phosphorylation sites
hyperkeratosis
cub deletion
curly bare
no stimulated shedding
substrate
decreased iRhom-ADAM17 binding efficency
increased constitutive shedding
substrate
14-3-3
14-3-3
increased degradation
Endolysosomal pathway

Figure S1

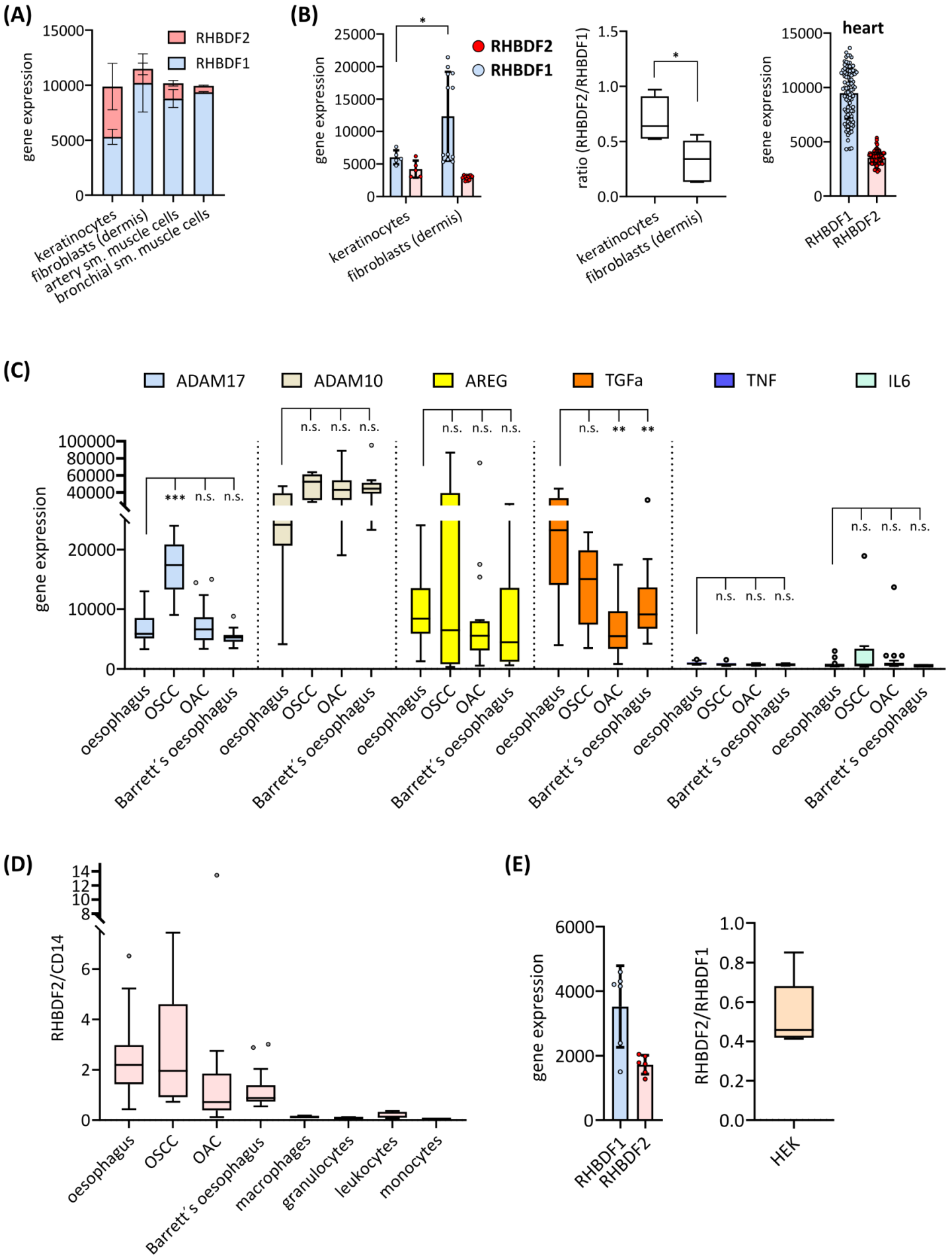
(A)
RHBDF2
RHBDF1
gene expression
keratinocytes
fibroblasts (dermis)
artery sm. muscle cells
bronchial sm. muscle cells
(B)
RHBDF2
RHBDF1
gene expression
ratio (RHBDF2/RHBDF1)
heart
keratinocytes
fibroblasts (dermis)
RHBDF1
RHBDF2
(C)
ADAM17
ADAM10
AREG
TGFa
TNF
IL6
gene expression
n.s.
***
**
oesophagus
OSCC
OAC
Barrett´s oesophagus
(D)
RHBDF2/CD14
oesophagus
OSCC
OAC
Barrett´s oesophagus
macrophages
granulocytes
leukocytes
monocytes
(E)
gene expression
RHBDF1
RHBDF2
RHBDF2/RHBDF1
HEK

Figure S2

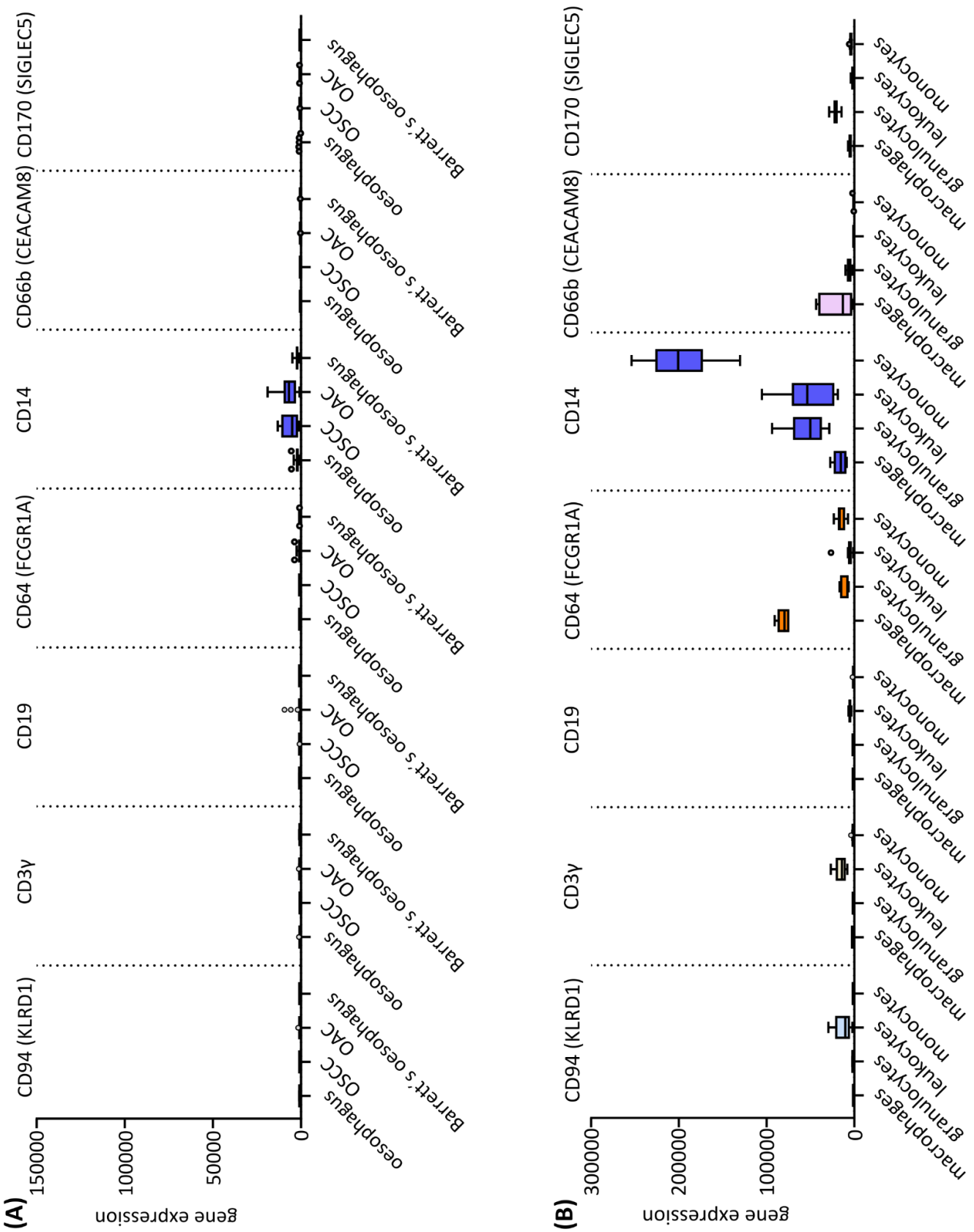
(A)
gene expression
150000
100000
50000
0
CD94 (KLRD1)
CD3γ
CD19
CD64 (FCGR1A)
CD14
CD66b (CEACAM8)
CD170 (SIGLEC5)
oesophagus
OSCC
OAC
Barrett's oesophagus
(B)
gene expression
300000
200000
100000
0
CD94 (KLRD1)
CD3γ
CD19
CD64 (FCGR1A)
CD14
CD66b (CEACAM8)
CD170 (SIGLEC5)
macrophages
granulocytes
leukocytes
monocytes

Figure S3

(A)

```
muiR2          1 MASADKNGSNLPSVSGSRLQSRKPPNLSITIPPP--ESQAPGEQDSMLPE----------
huiR2iso1      1 MASADKNGGSVSSVSSSRLQSRKPPNLSITIPPPEKETQAPGEQDSMLPEGFQNRRLKKS
huiR2iso2      1 MASADKNGGSVSSVSSSRLQSRKPPNLSITIPPPEKETQAPGEQDSMLPE----------
                 ********..:.***.*****************  *:************

muiR2         61 ------------------RRKNPAYLKSVSLQEPRGRWQEGAEKRPGFRRQASLSQSIRK
huiR2iso1     61 QPRTWAAHTTACPPSFLPKRKNPAYLKSVSLQEPRSRWQESSEKRPGFRRQASLSQSIRK
huiR2iso2     61 -------------------RKNPAYLKSVSLQEPRSRWQESSEKRPGFRRQASLSQSIRK
                                    ****************.****.:*****************
```

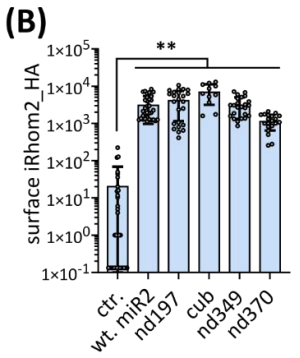

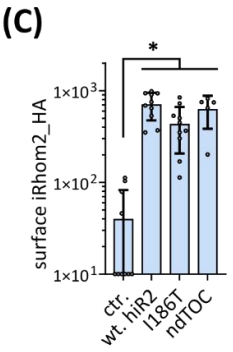

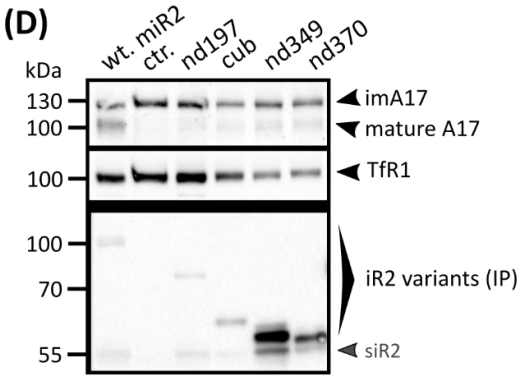

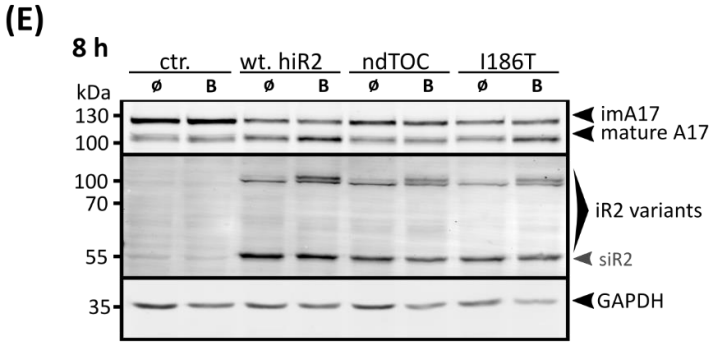

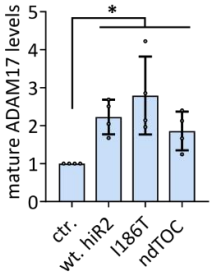

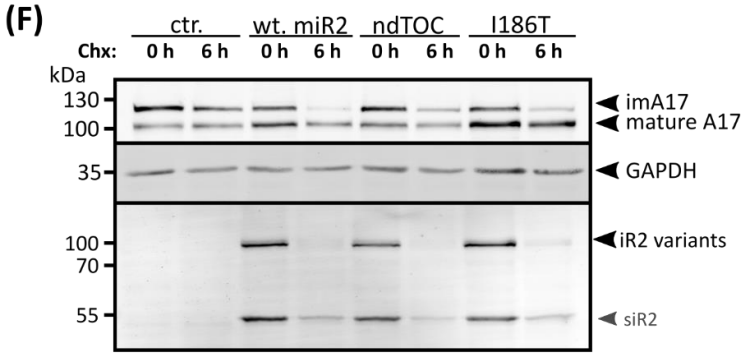

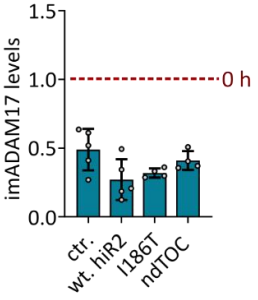

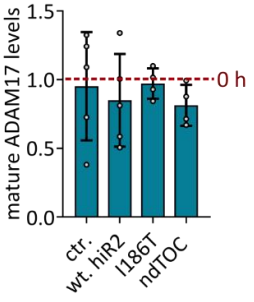

Figure S4

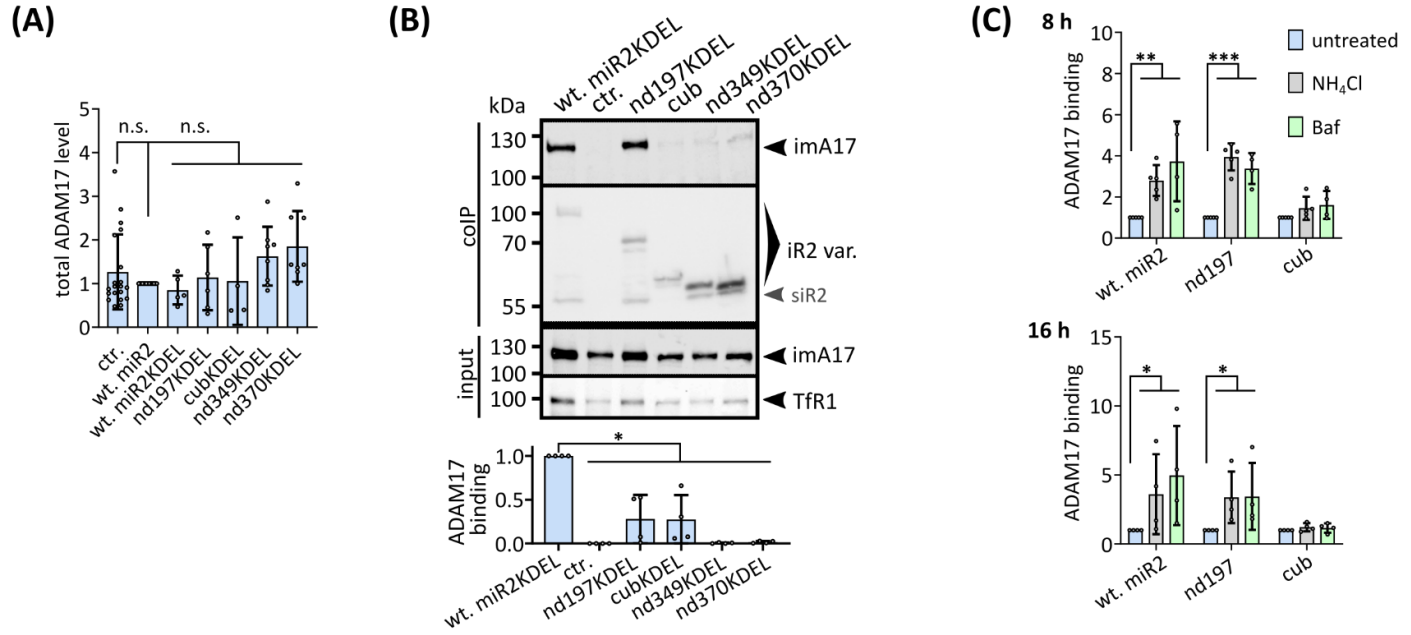
(A)
total ADAM17 level
n.s.
n.s.
ctr.
wt. miR2
wt. miR2KDEL
nd197KDEL
cubKDEL
nd349KDEL
nd370KDEL
(B)
kDa
wt. miR2KDEL
ctr.
nd197KDEL
cub
nd349KDEL
nd370KDEL
coIP
input
130
100
100
70
55
130
100
100
imA17
iR2 var.
siR2
imA17
TfR1
ADAM17 binding
*
(C)
8 h
16 h
ADAM17 binding
untreated
NH4Cl
Baf
**
***
*
*
wt. miR2
nd197
cub